

Basic Properties of Clusters of Galaxies and The Physics of the Intracluster Gas

CRAIG L. SARAZIN

Department of Astronomy

University of Virginia

P. O. Box 400325

Charlottesville, VA 22904-4325, USA

Summary. — Clusters of galaxies are the largest relaxed structures in the Universe, and have proven to be among the most important cosmological probes. They are composed of roughly 85% dark matter, 12% hot gas, and 3% stars and galaxies. In this chapter, the basic properties of clusters are reviewed. The physics of the intracluster gas is described in some detail. Gases at these temperatures (10^7 – 10^8 K) mainly emit X-rays. Many clusters of galaxies have central regions of dense, cooler intracluster gas called “cool cores.” The properties and physics of cool cores are reviewed. Clusters are formed hierarchically by mergers of smaller systems. The basic physics of cluster mergers is discussed. Finally, I describe the phenomena which occur when clusters with cool cores merge. Mergers may disrupt cool cores. Cool cores in merging clusters lead to sharp density discontinuities called “cold fronts” which have proven to be one of the most common features of high resolution Chandra images of clusters.

1. – Introduction

Clusters of galaxies are the largest relaxed, virialized systems in the Universe. They typically contain 10's to 100's of bright galaxies, and 1000's of fainter galaxies, in a region with a radius of ~ 2 Mpc. The largest clusters have total masses of $\sim 10^{15} M_{\odot}$. Clusters are typically somewhat ellipsoidal in shape. In terms of mass, the largest systems in the Universe form a continuum running from galaxies to groups of galaxies to clusters to superclusters and filaments. In galaxies, the inner parts of the dark matter potential are filled with stars. In groups and clusters, the stars are concentrated into galaxies. Supercluster and filaments are not generally relaxed systems. Clusters cover the total mass range of roughly $10^{14} M_{\odot}$ to $10^{15} M_{\odot}$. Typically, they have virial radii in the range of $r_{\text{vir}} \approx 1\text{--}3$ Mpc. Somewhat outdated reviews of the properties of clusters of galaxies are given in my book [1] and review article [2]. More recent reviews include [3, 4, 5], and, of course, the chapters in this volume.

Historically and at present, clusters are among the most important cosmological probes. In part, this is due to the fact that they occupy a unique and important intersection of physical scales. As mentioned above, they are the largest objects which are small enough to have come into dynamical equilibrium. Conversely, they are probably the smallest objects which are big enough to contain a fair sample of the materials in the Universe, particularly of baryonic and non-baryonic matter.

As cosmological probes, clusters provided some of the earliest and strongest evidence that we live in a low density Universe in which the matter density is too low to close the Universe [6], $\Omega_M \equiv \bar{\rho}/\rho_c \approx 0.3$, where $\bar{\rho}$ is the mean density of matter in the Universe, and $\rho_c \equiv 3H_0^2/(8\pi G)$ is the critical density.

This chapter presents material from three lectures at the Enrico Fermi School “Astrophysics of Galaxy Clusters” at Villa Monastero in Varenna, Italy on 15-25 July 2008. The three lectures were entitled “The Properties of Clusters and Our Basic Theoretical Understanding,” “The Physics of the Intracluster Gas,” and “Cool Cores in Cluster, Cluster Mergers, and Outstanding Questions about Clusters.” The material in these three lectures have been combined in this one chapter.

As much as possible, comparisons to observations in this chapter assume the standard WMAP cosmology [7], with a Hubble constant of $H_0 = 71 \text{ km s}^{-1} \text{ Mpc}^{-1}$, a ratio of the mass density to the critical density of $\Omega_M = 0.27$, and the ratio of the dark energy density to the critical density of $\Omega_{\Lambda} = 0.73$.

2. – Properties of Clusters and Our Basic Theoretical Understanding

2.1. Dark Matter in Clusters. – Although historically clusters were first seen as strong concentrations of galaxies in the optical, we now know that galaxies and stars form a small fraction of the mass of clusters ($\sim 3\%$). Most of the visible baryonic mass is hot intracluster gas ($\sim 12\%$ of the total mass). The bulk of the mass is in dark matter (DM), which typically contains $\sim 85\%$ of the mass [8, 3, 9]. The proportions of baryonic and dark matter in clusters are similar to those determined from measurements of the

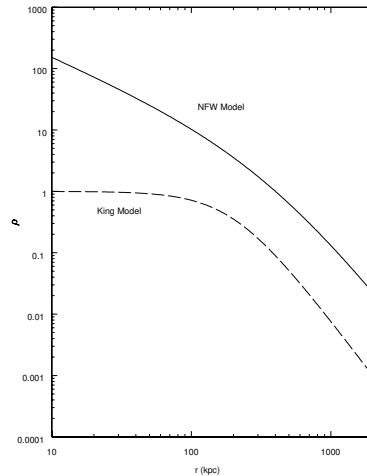


Fig. 1. – Solid curve shows an NFW (eq. 1, [14]) density profile with a scaling radius of $r_s = 400$ kpc. The dashed curve is the analytic “King” density profile with a core radius of $r_c = 200$ kpc. The density scales are arbitrary.

Cosmic Microwave Background [7]. Clusters were the first extragalactic systems which were found to be dominated by dark matter [10, 3], and have provided some of the earliest and strongest evidence that we live in a Universe in which the mass is predominately dark matter [8, 3].

Clusters have also provided some of the strongest and most direct evidence about the nature of dark matter. The X-ray, galaxy, and weak lensing distributions in the merging Bullet Cluster 1E0657–56 have shown that the gravitational lensing is centered on the distribution of galaxies, rather than hot gas distribution [11, 12, 13]. Since the majority of the baryons are in the hot gas, this indicates that most the mass in the cluster, which is due to dark matter, must be non-baryonic. During a merger, the gas motion is impeded by ram pressure forces, since the gas is a collisional fluid. The galaxies are nearly collisionless. The fact that the dark matter moves in the same manner as the galaxies indicates that the dark matter is made up of collisionless particles. Also, the dark matter cannot have large, nongravitational motions; the majority of the dark matter must be “cold”. This is completely consistent with the Cold Dark Matter (CDM) hypothesis which is the basis for much of our current understanding of cosmology, large-scale structure, and extragalactic astronomy [3].

2.1.1. Spatial Distribution of Dark Matter in Clusters. Numerical simulations suggest that the dark matter distribution in clusters should have a power-law drop off at large radii, and a flatter power-law at small radii [14]. Thus, the dark matter distribution should have a cusp at the center of the cluster. The NFW dark matter profile (fig. 1,

[14]) has

$$(1) \quad \rho_{\text{DM}}(r) = \rho_s \left[\left(\frac{r}{r_s} \right) \left(1 + \frac{r}{r_s} \right)^2 \right]^{-1},$$

where r_s and ρ_s are the characteristic scaling radius and density, respectively. The DM mass in a clusters within a radius r is then

$$(2) \quad M_{\text{DM}}(r) = 4\pi\rho_s r_s^3 \left[\ln \left(1 + \frac{r}{r_s} \right) - \left(\frac{r}{r + r_s} \right) \right].$$

It is useful to define a concentration parameter c as $c \equiv r_{\text{vir}}/r_s$, where r_{vir} is the virial radius of the cluster. Typically, $c \approx 5$ for clusters, and rough values of the radii are $r_{\text{vir}} \sim 2$ Mpc and $r_s \sim 400$ kpc.

The NFW profile is consistent with mass distributions derived from the distribution of the hot gas, from the galaxy distributions and velocities, and from weak gravitational lensing [15, 16].

2.1.2. Sizes of Clusters. The NFW profile (or any other self-similar DM profile) depends on the scale density ρ_s and the scale radius $r_s = r_{\text{vir}}/c$. For a cluster of a given mass, eq. (2) can be used to determine the the scale density ρ_s if the size of the cluster is known. However, one needs to know the virial radius r_{vir} (or scale radius $r_s = r_{\text{vir}}/c$ of the cluster.

There is a simple argument which gives the sizes of clusters with moderate accuracy. This simple picture is sometimes called the ‘‘Spherical Top Hat’’ model. In this model, one treats the formation of a cluster as equivalent to the collapse of a isolated, spherical region of overdensity in the Universe. By Birkhoff’s Theorem, the gravitational field only depends on the mass interior to the radius for any spherical solution. Thus, one can treat the cluster as an individual ‘‘universe’’. In the Top Hat model, one assumes further that the density within the protocluster is uniform. Then, in the absence of dark energy, such a perturbation evolves in the same way as a universe with the same density would evolve. The perturbation in density associated with the protocluster will grow in time, and will collapse when the density within the perturbation reaches the critical density at that time,

$$(3) \quad \rho = \rho_{\text{crit}}(z_f) \equiv \frac{3H^2(z_f)}{8\pi G}.$$

where z_f is the redshift at which the cluster forms, and $H(z_f)$ is the value of the Hubble constant at that redshift. If the cluster density is uniform, then the entire cluster will collapse at the same instant, and the protocluster will be stationary at the moment when the whole cluster turns around and collapses. Then, its energy is purely potential energy, and is given by $E = -(3/5)GM^2/r_m$, where r_m is the maximum radius of the protocluster (the value at turnaround). After the cluster has recollapsed and virialized, the Virial Theorem implies that the energy will be $E = (1/2) \text{PE} = - \text{KE}$, where PE

and KE are the potential and kinetic energy, respectively. Combining this result with the standard Einstein–deSitter cosmological solution implies that the average density within the virial radius of the cluster is

$$(4) \quad \langle \rho(< r_{\text{vir}}) \rangle = \Delta_v \rho_{\text{crit}}(z_f) = 18\pi^2 \rho_{\text{crit}}(z_f) \approx 180 \rho_{\text{crit}}(z_f).$$

The previous arguments don't apply exactly to a universe with dark energy, but the result for a flat universe with a cosmological constant is [17]

$$(5) \quad \Delta_v \approx 18\pi^2 - 82\Omega_\Lambda - 39\Omega_\Lambda^2.$$

Thus, $\Delta_v \rho_{\text{crit}}(z_f) = 3M/(4\pi r_{\text{vir}}^3)$. Then, the virial radius of a cluster is given by

$$(6) \quad r_{\text{vir}} = \left[\frac{3M}{4\pi \Delta_v \rho_{\text{crit}}(z_f)} \right]^{1/3} \propto M^{1/3} [\rho_{\text{crit}}(z_f)]^{-1/3} \approx 2.6 \left[\frac{M}{10^{15} M_\odot} \right]^{1/3},$$

where the latter numerical value applies to the present-day Universe, $z_f = 0$.

One should note that a number of different cluster radii are in common use. For example, there are versions of the virial radius based on the argument given above, which are often written as r_{180} or r_{200} , where, for example, $\langle \rho(< r_{200}) \rangle \equiv 200 \rho_{\text{crit}}$. There are also similar values scaled to the current mass density of the Universe, $\rho_m = \Omega_M \rho_{\text{crit}}$, rather than the critical density. Smaller radii more appropriate to studies of the central regions of clusters are also often used; examples are r_{2000} or r_{500} , where, for example, $\langle \rho(< r_{500}) \rangle \equiv 500 \rho_{\text{crit}}$.

In general, for any given definition of the radius of a cluster, one expects that the radius will scale approximately with the mass as $r \propto M^{1/3}$.

2.2. Galaxy Content of Clusters. – Although they represent only a small fraction of the mass of clusters, galaxies are the component of clusters which was observed first. The term “richness” is often used to denote a measure of the total number of galaxies or total mass of galaxies in a cluster.

The individual galaxies in clusters have a range of masses and luminosities, with the brightest and most luminous galaxies being less common than the less massive galaxies. The distribution of galaxies with different luminosities is described by the luminosity function $n(L_{\text{opt}})$, where $n(L_{\text{opt}}) dL_{\text{opt}}$ gives the number of galaxies with optical luminosities in the range L_{opt} to $L_{\text{opt}} + dL_{\text{opt}}$. In many cases, galaxy luminosity functions are approximated by the Press-Schechter function [18]

$$(7) \quad n(L_{\text{opt}}) dL_{\text{opt}} = N^* \left(\frac{L_{\text{opt}}}{L^*} \right)^{-\alpha} \exp \left(-\frac{L_{\text{opt}}}{L^*} \right) dL_{\text{opt}},$$

where L^* is a characteristic luminosity of the galaxies, and N^* is a measure of the richness of the cluster. Typical values of exponent are $\alpha \approx 1.25$. For $\alpha \geq 1$, the total number of

galaxies formally diverges as $L_{\text{opt}} \rightarrow 0$. However, the total galaxy luminosity normally converges.

Rich clusters primarily contain “early-type” galaxies, which are elliptical (E) and lenticular (S0) galaxies. Clusters are deficient in spiral (Sp) galaxies, particularly near their centers. Another way of characterizing the galactic population of clusters is that the galaxies mainly contain a very old stellar population; the elliptical galaxies in clusters are often described as “red and dead”. This implies that these galaxies contain mainly old, low mass ($\lesssim 1 M_{\odot}$), red stars, and have very low rates of current star formation.

Clusters of galaxies often contain very large elliptical galaxies, which are located very near the centers of relaxed clusters. These galaxies generally referred to as “brightest cluster galaxies” (BCGs). Some of the BCGs are cD galaxies, which have very extensive outer envelopes. The cD galaxies have very large luminosities $L_{\text{opt}} \gtrsim 10L^*$, which are unlikely to occur given the normal galaxy luminosity function (eq. 7). It is generally assumed that these galaxies form at the centers of dense regions in the early Universe, and that they are produced by the merger of smaller galaxies. Although these BCGs are elliptical galaxies in clusters, they are also unusual in that a fraction of them (those at the centers of cool core clusters) contain significant masses of cooler gas and have large star formation rates. These cool core BCGs are discussed in more detail below in § 4.

In addition to the stars located in galaxies, clusters contain a population of intracluster stars which were probably stripped from galaxies.

The velocities of galaxies in clusters have a complex distribution, but in regular clusters the observed distributions of line-of-sight velocities are roughly gaussian in form. The distribution can be characterized by the radial velocity distribution σ_{gal} . Typical values are $\sigma \sim 1000 \text{ km s}^{-1}$.

The spatial distributions of galaxies can generally be represented by the NFW form (eq. 1, fig. 1). In clusters with a central BCG, it probably is more sensible to discuss the distribution of galaxy mass or luminosity, rather than that of galaxy number, since this one galaxy is much brighter than typical galaxies and may have formed by accreting other galaxies. In the past, galaxy distributions in clusters were often modeled using a function with a constant density core (fig. 1),

$$(8) \quad n_{\text{gal}}(r) = n_{\text{gal},0} \left[1 + \left(\frac{r}{r_c} \right)^2 \right]^{-3/2},$$

where $n_{\text{gal},0}$ is the central galaxy number density and r_c is the core radius. Typically, $r_c \approx r_s/2 \approx 200 \text{ kpc}$. However, the small number of bright galaxies near the center of a cluster means that the center is difficult to determine accurately. If the actual galaxy distribution has a cusp like the NFW profile but the center is located inaccurately, the resulting projected profile will appear to have a core. In a cluster with a BCG very near the cluster, its center can be used to estimate the center of the galaxy distribution, but as noted above, it is probably more sensible to discuss the distribution of stellar luminosity rather than galaxy number in clusters with a BCG. In this case, clusters with a center

BCG will generally have a cuspy distribution in the luminosity distribution due to the BCG.

2.3. Intracluster Medium. – The intracluster medium (ICM) consists of a mix of thermal plasma, magnetic fields, and relativistic particles which fill the space within clusters.

One of the more surprising results from X-ray astronomy is that the great volumes of space between galaxies in clusters of galaxies are not empty, as they appear in optical images. Instead, they are filled with a diffuse, hot plasma, with typical temperatures of $T \sim 10^7 - 10^8$ K, which gives thermal energies of $kT \sim 1 - 10$ keV. At this temperature, the sound speed in the gas is comparable to the orbit velocities of the galaxies in the cluster, which is consistent with the gas being in hydrostatic equilibrium with the same gravitational potential as binds the galaxies. This intracluster medium is highly rarefied, with electron number densities of $n_e \sim 10^{-4} - 10^{-2}$ cm⁻³. At least on large scales, the gas is stably stratified, with the density decreasing with increasing radius r . The gas extends out to distances of $r \gtrsim 2$ Mpc from the cluster center. The total mass of hot gas is typically $M_{\text{gas}} \sim 10^{14} M_{\odot}$; this mass exceeds the total mass of all the galaxies in a typical rich clusters, although even more of the mass is in the form of dark matter. The gas consists primarily of hydrogen and helium, but also contains heavier elements (e.g., oxygen and iron) with abundances which are roughly one third of those in the Sun.

At temperatures of $10^6 - 10^8$ K, the dominant radiation mechanism of a plasma is X-ray emission. As a result, clusters of galaxies are generally very luminous X-ray emitters, with luminosities of $L_X \sim 10^{43} - 10^{45}$ ergs s⁻¹. Clusters are second only to quasars as the most luminous X-ray sources in the Universe, and are the most luminous extended sources. While X-ray emission is the primary observational diagnostic for the intracluster medium, the ICM has a number of other important physical effects. It confines and distorts radio galaxies within the cluster. The cosmic ray and magnetic field components of the intracluster medium can also produce diffuse radio emission. The ICM can strip interstellar gas from galaxies as they move through the cluster. Intracluster gas cools at the centers of many clusters, producing lower temperature gas. If the ICM contains dust, the dust will be strongly heated by the plasma, and may emit strongly in the infrared. The ICM also has a number of opacity effects; for example, it scatters and heats the cosmic background radiation which passes through it. The magnetic field in the ICM leads to Faraday rotation and depolarization (§ 3.3.2).

2.4. The Mass Function of Clusters. – Clusters of galaxies are rare, massive objects in the Universe. The greater the mass of the cluster, the rarer they are. How many clusters are there, and how does their number density depend on their mass? The integrated mass function of clusters $n(M, z)$ is defined such that $n(M, Z)$ gives the number of clusters with mass $\geq M$ per unit volume at redshift z . Usually, the mass function is defined per comoving volume, which removes the effect of the expansion of the Universe. At present, the best theoretical determinations of the mass function come from numerical simulations. However, there is a simple argument which gives the shape and

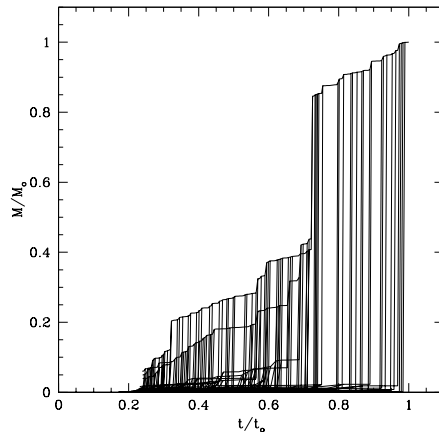


Fig. 2. – Example of a cluster merger tree from [19]. The figure gives the accumulation of the mass M as a fraction of the final cluster mass $M_0 = 10^{15} h^{-1} M_\odot$ as a function of the cosmic time as a fraction of the current age of the Universe. This tree was computed for an open model Universe ($\Omega_M = 0.3$, $\Omega_\Lambda = 0$).

normalization of the mass function with reasonable accuracy. This Press-Schechter (PS) mass function [18] assumes that clusters and all other large structures grow from small density fluctuations in the early Universe, and that these fluctuations have a gaussian distribution. The size of the fluctuations can be characterized by $\sigma_M(z)$, which gives the variance in the density and thus amplitude of the fluctuation field when averaged on spatial scales which correspond to an average mass of M . The PS formalism assumes that the fluctuations are larger on smaller scales, so that $\partial\sigma_M/\partial M < 0$. The spherical Top Hat model (§ 2.1.2) is used to calculate the collapse of individual fluctuations. Thus, individual fluctuations collapse when their density has grown to exceed the critical density $\rho_{\text{crit}}(z)$ at that epoch. It is easier to treat the evolution of the spectrum of fluctuations in the linear limit when they are very small, and use the Top Hat approximation to deal with the non-linear evolution. Thus, one defines δ_c as the critical linear overdensity for collapse. In an Einstein-deSitter universe, the critical overdensity is

$$(9) \quad \delta_c = \frac{3}{5} \left(\frac{3\pi}{2} \right)^{2/3} \approx 1.69.$$

For other cosmologies, δ_c depends on the redshift z and the cosmology. With these assumptions, the Press-Schechter differential mass function is given by

$$(10) \quad \frac{dn(M, Z)}{dM} = \sqrt{\frac{2}{\pi}} \frac{\bar{\rho}}{M^2} \frac{\delta_c}{\sigma_M(z)} \left| \frac{d \log \sigma_M(z)}{d \log M} \right| \exp \left[-\frac{\delta_c^2}{2\sigma_M^2(z)} \right],$$

where $\bar{\rho}$ is the mean density of the Universe at the present epoch.

The amplitude of the fluctuation spectrum is usually characterized by giving σ_8 which is the present value of $\sigma_M(z=0)$ on a spatial scale of $8h^{-1}$ Mpc. Here, $h \equiv (H_0/100 \text{ km s}^{-1} \text{ Mpc}^{-1})$. Over a narrow range of scales, the power spectrum of fluctuations is well-represented as a power-law, $P(k) \propto k^n$, where k is the wavenumber. Then, the amplitude of the fluctuations on a mass scale M is $\sigma_M = \sigma_8(M/M_8)^\alpha$, where M_8 is the average mass contained in a scale of $8h^{-1}$ Mpc, and $\alpha = (n+3)/6$.

Because of the exponential term in eq. (10), the mass function falls off very rapidly with increasing mass for the large masses of clusters. As a result of this, the number density of clusters should depend very strongly on redshift and cosmology, and is exquisitely dependent on the amplitude of fluctuations, σ_8 . This means that the abundance of clusters provides a very strong test of cosmology and large scale structure (e.g., [3]).

2.5. The Formation of Clusters — Mergers and Accretion. — Clusters of galaxies form hierarchically, with smaller objects (galaxies and groups of galaxies) forming first. Gravity pulls these objects together to form clusters. Simulations of large scale structure formation show that in the standard Lambda CDM cosmology, clusters mainly form within filaments of enhanced density, and that the largest clusters often form at the intersection of these filaments. Clusters form through a mixture of more common mergers with small objects, and rarer mergers with larger clusters. Figure 2 shows the merger history of a large simulated cluster. Clearly there are both large and small mergers. It is conventional to divide these effects into “major mergers” (say, mass ratios greater than 1:3) and minor mergers or “accretion” (smaller mass ratios. Figure 2 also illustrates that clusters have formed in the past, but are also forming currently.

Obviously, the formation of clusters and their merger histories are most accurately treated within full cosmological simulations of large-scale structure. However, as was true with the Press-Schechter mass function of clusters (eq. 10), there are simple analytic arguments which capture many of the essential features of cluster merger histories (e.g., [20]). Generally, one makes the same assumptions as motivated the Press-Schechter mass function (eq. 10), and additionally posits that when two DM halos are contained within a larger halo, and that large halo reaches the critical density, then the two halos merge into the larger halo. With these assumptions, the merger rate of clusters of mass M merging with clusters of mass $M' - M$ to form a cluster in the mass range M' to $M' + dM'$ is given by

$$(11) \quad \text{Rate}(M \rightarrow M', t) dM' = \sqrt{\frac{2}{\pi}} \left| \frac{d\delta_c(t)}{dt} \right| \frac{1}{\sigma_{M'}^2} \left| \frac{d\sigma_{M'}}{dM'} \right| \left(1 - \frac{\sigma_{M'}^2}{\sigma_M^2} \right)^{-3/2} \\ \times \exp \left[-\frac{\delta_c^2(t)}{2} \left(\frac{1}{\sigma_{M'}^2} - \frac{1}{\sigma_M^2} \right) \right] dM'.$$

Figure 2 shows an example of a merger tree calculated with eq. (11) from [19].

Major cluster mergers are remarkable collisions; they are the most energetic events in the Universe since the Big Bang. During a major merger of two large clusters (each with a mass $\sim 10^{15} M_\odot$) merging at a relative velocity of $\sim 2000 \text{ km s}^{-1}$, the total energy

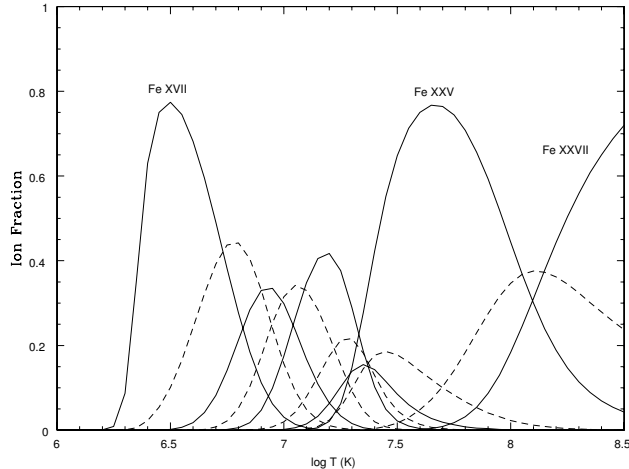


Fig. 3. – Ionization fractions of iron ions from Fe XVII (Fe^{+16}) to Fe XXVII (Fe^{+16} , fully stripped iron) as a function of temperature in collisional ionization equilibrium. The ions with even charges have solid curves, while the ions with odd charges have dashed curves. Note that the gas becomes more ionized as the temperature increases.

released is $\sim 2 \times 10^{64}$ ergs, of which $\sim 2 \times 10^{63}$ ergs may be dissipated in the intracluster gas by merger shocks.

3. – Physics of the Intracluster Gas

In this chapter, I will review the physical state and X-ray emission processes of the ICM (§ 3.1 & 3.2). The ICM is shown to act as a fluid in § 3.3. In § 3.4, the transport properties of the gas, particularly thermal conduction, are discussed. The hydrodynamical equations for the ICM are given in § 3.5. Models for the distribution of the gas, and the use of the gas to determine the total mass distributions of clusters are described in §§ 3.6 and 3.6.4. The heating and cooling processes in the ICM are discussed in § 3.7.

3.1. Physical State of the Intracluster Gas: Local Thermal State. – At the very high temperatures of the intracluster gas, the gas is very highly ionized, but not completely so for the heavy elements. Thus, to describe the local thermal state of the gas, we need to specify three things. First, there are the motions of free particles (electrons and ions), or the kinetic state of the gas. Then, we need to give the ratios of electrons which are free to those which are bound to ions, or the ionization state of the gas. Finally, for the bound electrons, we need to which energy levels they occupy; this is the excitation state of the gas.

3.1.1. Kinetic Equilibrium. If Coulomb collisions are sufficiently rapid, the free particles in the gas (free electron, free proton, and ions) will be brought into kinetic equilibrium

and develop a Maxwellian distribution. The time scale for a particle of mass m_1 and charge $Z_1 e$ to collide with field particles of mass m_2 and charge $Z_2 e$ with a number density of n_2 in a Maxwellian distribution at a temperature T is [21]

$$(12) \quad t_{\text{eq}}(1, 2) = \frac{3m_1 \sqrt{2\pi} (kT)^{3/2}}{8\pi \sqrt{m_2} n_2 Z_1^2 Z_2^2 e^4 \ln \Lambda}.$$

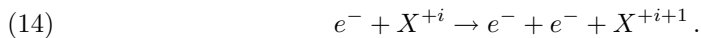
Here, $\ln \Lambda \equiv \ln(b_{\text{max}}/b_{\text{min}}) \approx 40$ is the Coulomb logarithm, and b_{min} and b_{max} are the minimum and maximum impact parameters for Coulomb collisions in the gas. The Coulomb logarithm has a weak (logarithmic) dependence on density and temperature, but is nearly constant under ICM conditions. Coulomb collisions between electrons will bring the electrons into equilibration (an isotropic Maxwellian velocity distribution) on a time scale of roughly

$$(13) \quad t_{\text{eq}}(e, e) \approx 2 \times 10^5 \text{ yr} \left(\frac{T}{10^8 \text{ K}} \right)^{3/2} \left(\frac{n_e}{10^{-3} \text{ cm}^{-3}} \right)^{-1} \text{ yr}.$$

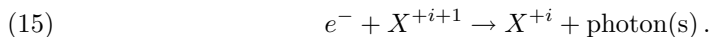
The time scale for protons to equilibrate among themselves is $t_{\text{eq}}(p, p) \approx (m_p/m_e)^{1/2} t_{\text{eq}}(e, e)$, or roughly 43 times longer than the value in eq. (13). Following this time, the protons and ions would each have Maxwellian distributions, but generally at different temperatures. The time scale for protons to collide with electrons and exchange energy is $t_{\text{eq}}(p, e) \approx (m_p/m_e) t_{\text{eq}}(e, e)$, or roughly 1870 times the value in eq. (13). The time scale for the electrons and protons to come into equipartition (equal temperatures) is roughly one half of $t_{\text{eq}}(p, e)$ [21].

Under typical conditions in the intracluster gas, these time scales are $t_{\text{eq}}(e, e) \sim 10^5$ yr, $t_{\text{eq}}(p, p) \sim 4 \times 10^6$ yr, and $t_{\text{eq}}(p, e) \sim 2 \times 10^8$ yr. Most clusters have existed for $\gtrsim 10^9$ yr, so one would expect the gas to generally be in kinetic equilibrium, with the distributions of free particles being isotropic Maxwellians. Moreover, the electrons and ions should generally be in equipartition, with a common kinetic temperature $T = T_e = T_p$. Possible exceptions might be the outermost regions of clusters (where the gas density is low), or regions where the gas properties have changed rapidly, such as shocks [22].

3.1.2. Collisional Ionization Equilibrium. The main ionization process in the intracluster gas is collisional ionization,



The main recombination processes are radiative and dielectronic recombination,



Here, X^{+i} represents some element X which has been ionized i times. Note that neither radiative nor dielectronic recombination (eq. 15) are the inverse of collisional ionization

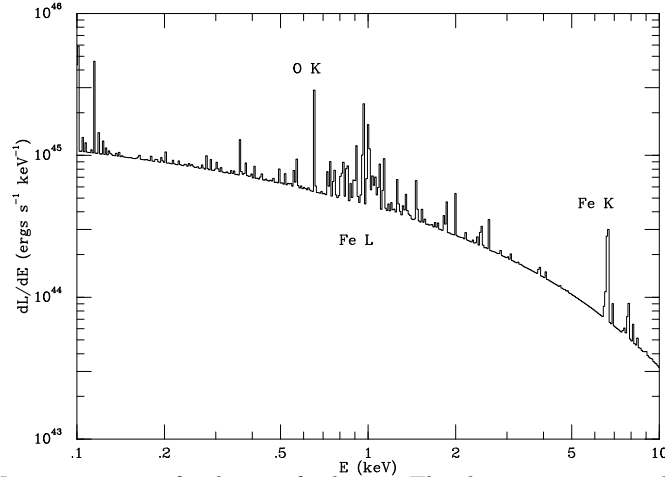


Fig. 4. – Model X-ray spectrum of a cluster of galaxies. The cluster was assumed to be isothermal at $T = 8 \times 10^7$ K in its outer regions, and to have a large amount of cool gas (a cool core) in its inner regions.

(eq. 14), which implies that the ionization state in the intracluster gas is not that in thermodynamic equilibrium (the Saha equation).

Let $C(X^i, T)$ be the rate coefficient for collisional ionization out of the ion X^i (eq. 14), while $\alpha(X^i, T)$ is the rate coefficient for recombination to the ion X^i (eq. 15). If the gas starts in a lower ionization state than in equilibrium, it will be ionized up towards equilibrium on a time scale of roughly

$$(16) \quad t_{\text{ion}} \approx [C(X^i, T)n_e]^{-1} \approx 3 \times 10^8 \left[\frac{C(X^i, T)}{10^{-13} \text{ cm}^3 \text{ s}^{-1}} \right]^{-1} \left(\frac{n_e}{10^{-3} \text{ cm}^{-3}} \right)^{-1} \text{ yr}.$$

In general, the collisional ionization rates are high enough that one would expect the ICM to usually be in collisional ionization equilibrium. Again, possible exceptions might be the outermost regions of clusters (where the gas density is low), or regions where the gas properties have changed rapidly, such as shocks.

In collisional ionization equilibrium, the rates of collisional ionization and radiative and dielectronic recombination balance, which implies that

$$(17) \quad [C(X^i, T_g) + \alpha(X^{i-1}, T_g)] n(X^i) = C(X^{i-1}, T_g)n(X^{i-1}) + \alpha(X^i, T_g)n(X^{i+1}).$$

Here, $n(X^i)$ is the number density of the X^i ion. Note that, unlike thermodynamic equilibrium (Saha equilibrium), the state of ionization in collisional ionization equilibrium is independent of density, and only depends on the electron kinetic temperature T . The ionization fractions of highly ionized species of iron are shown as a function of the temperature in fig. 3. Generally, the fraction of each ion reaches a maximum at a

temperature that is some fraction of its ionization potential. At the temperatures which predominate in clusters, iron is mainly in the fully stripped, hydrogenic, or heliumlike stages.

3.1.3. Excitation Equilibrium. For ions with bound electrons, the population of excited states are determined mainly by a balance between collision excitation by free electrons and radiative de-excitation. In general, the spontaneous radiative de-excitation rates are much higher than the excitation rates, and the electrons are almost always found in the ground level. The population of excited states are much lower than would be expected in thermodynamic equilibrium (Boltzmann distribution). Collisional de-excitation rates are much lower than radiative de-excitation rates; this means that there are no X-ray spectral diagnostics which determine the local density in the gas.

3.2. X-ray Emission. – The X-ray emission of the intracluster gas is mainly due to thermal bremsstrahlung and line emission. There are smaller contributions of continuum from bound-free (recombination) emission and from two-photon decays of 2s levels in hydrogenic and helium-like ions.

The emissivity due to thermal bremsstrahlung (free-free emission) is given by

$$(18) \quad \epsilon_{\nu}^{ff} = \frac{2^5 \pi e^6}{3 m_e c^3} \left(\frac{2\pi}{3 m_e k} \right)^{1/2} n_e T^{-1/2} \exp(-h\nu/kT) \sum_i Z_i^2 n_i g_{ff}(Z_i, T, \nu),$$

where the emissivity ϵ_{ν} is defined as the emitted energy per unit time, frequency, and volume. The sum is over the various ions in the plasma, but is dominated by hydrogen and helium for Solar abundances. The Gaunt factor $g_{ff}(Z_i, T, \nu)$ corrects for quantum mechanical effects and for the effect of distant collisions, and is a slowly varying function of frequency and temperature. As a result, the dominant dependence of the free-free emissivity on frequency is the Boltzmann exponential factor, and the main dependences on temperature are this factor and the square-root factor $T^{-1/2}$. Thermal bremsstrahlung produces a roughly exponential continuum component in the X-ray spectrum. At high temperatures $T \gtrsim 3 \times 10^7$ K, thermal bremsstrahlung is the dominant emission mechanism.

At lower temperatures, the main X-ray radiation is from lines. The strongest line feature observed from most clusters of galaxies is the complex of iron Fe K α lines at about 6.7 keV. This line feature is actually a blend of lines from iron ions (mainly Fe⁺²⁴ and Fe⁺²⁵) and weaker lines from nickel ions. The notation “K α ” gives the principal quantum number n of the lower level of the transition and the change in the principal quantum number $\Delta n \equiv n' - n$, where n' is the principal quantum number of the upper level of the transition. K indicates that the lower level is in the K-shell ($n = 1$), L indicates the lower level is in the L-shell ($n = 2$), and so on, while α indicates that $\Delta n = 1$, β indicates that $\Delta n = 2$, etc. In addition to the Fe K line complex, the X-ray spectra of clusters of galaxies contain a large number of lower energy lines. These include the K lines of the common elements lighter than iron, such as C, N, O, Ne, Mg, Si, S,

Ar, and Ca, as well as the L lines of Fe and Ni. These lines become very strong at lower temperatures ($T \lesssim 10^7$ K),

As an illustration, Figure (4) shows the predicted X-ray spectrum of an X-ray cluster [23]. The model cluster is isothermal in its outer regions (with a temperature of 8×10^7 K), and has a cool core at its center. The figure shows the overall exponential continuum from thermal bremsstrahlung, the Fe K lines at about 7 keV (which come mainly from the region of the cluster outside of the cool core), and the lower energy lines from the cool core.

Most X-ray lines are excited by collisional excitation by electrons, although radiative and dielectronic recombination and inner shell collisional ionization also play a role. The emissivity due to a collisionally excited line is usually written [24]

$$(19) \quad \int \epsilon_\nu^{\text{line}} d\nu = n(X^i)n_e \frac{h^3 \nu \Omega(T) B}{4\omega_{gs}(X^i)} \left[\frac{2}{\pi^3 m_e^3 kT} \right]^{1/2} e^{-\Delta E/kT},$$

where $h\nu$ is the energy of the transition, ΔE is the excitation energy above the ground state of the excited level, B is the branching ratio for the line (the probability that the upper state decays through this transition), and Ω is the ‘collision strength’, which is often a slowly varying function of temperature.

The intracluster gas is almost certainly in collisional ionization equilibrium (§ 3.1.2); under these circumstances, the ionization fractions depend only on the electron temperature T , and are independent of the density of the gas. Then, the density of any ion is just proportional to the proton density in the gas times the abundance of the relevant element relative to hydrogen. Thus, all of the X-ray emission processes in the gas scale with the product $n_p n_e$ of the proton and electron densities, respectively. If L_ν is the X-ray luminosity per unit frequency emitted by a cluster, then this can be written as

$$(20) \quad L_\nu = \Lambda_\nu(T, \text{Abundances}) \int n_e n_p dV,$$

where the integral is over the volume V of the cluster. The emissivity is $\epsilon_\nu = \Lambda_\nu n_e n_p$, where Λ_ν depends only on the temperature and the abundances of the heavier elements relative to hydrogen. Similarly, the X-ray surface brightness is given by

$$(21) \quad I_\nu = \Lambda_\nu(T, \text{Abundances}) \int n_e n_p dl.$$

Here, the integral is along the line of sight distance l through the cluster.

The emissivity of a line is then proportional to the square of the density and to the abundance of the relevant element, and depends significantly on the electron temperature. Because the thermal bremsstrahlung emissivity also is proportional to the square of the density (eq. 18), the ratio of line emission to thermal bremsstrahlung continuum emission is independent of density. Line ratios or the shape of the X-ray continuum spectrum can be used to derive a temperature for the gas in a cluster. Then, the ratio of line emission

to thermal bremsstrahlung continuum emission can be used to determine the abundance of the heavy element responsible for the line.

3.3. *The Intracluster Medium as a Fluid.* –

3.3.1. Mean Free Paths. The mean free paths of electrons and ions in a plasma without a magnetic field are determined by Coulomb collisions [21]. The electrons in a Maxwellian plasma undergo Coulomb collisions in a time which is a factor of $\sqrt{m_e/m_p}$ shorter than the protons (§ 3.1.1). On the other hand, the electrons move faster by the inverse of this factor. Thus, the mean free paths of electrons and protons are essentially equal, with

$$(22) \quad \lambda_p = \lambda_e = \frac{3^{3/2}(kT)^2}{4\pi^{1/2}n_e e^4 \ln \Lambda} \approx 23 \left(\frac{T}{10^8 \text{ K}} \right)^2 \left(\frac{n_e}{10^{-3} \text{ cm}^{-3}} \right)^{-1} \text{ kpc}.$$

These mean free paths are smaller than most scales of interest in clusters; they are only about 1% of the radius of a cluster (~ 2 Mpc). Thus, it is reasonable to treat the ICM as a fluid under most circumstances. The fluid approximation might breakdown in the outer parts of a cluster (where the lower density increases λ_e), in interactions with galaxies (whose sizes are comparable to λ_e), if the ICM is very inhomogeneous, or in sharp transitions in the ICM properties at shocks or cold fronts (§ 5.3 & 6.2).

3.3.2. Magnetic Fields and Gyroradii. In any case, the ICM apparently contains a significant magnetic field, with typical values of $B \sim 1 \mu\text{G}$. (See the chapter by Rephaeli for more details concerning the magnetic field in clusters.) Stronger fields occur in some smaller volumes of clusters. These fields are probably too weak to be very important dynamically, as the magnetic pressure, $P_B = B^2/(8\pi)$, is much smaller than the typical gas pressures. However, the magnetic field does very strongly effect the microscopic motions of electrons and ions. In the presence of a magnetic field, electrons and ions follow helical orbits, gyrating about magnetic field lines. The gyroradii of electrons and ions in cluster magnetic fields are very small. For example, the gyroradius of a typical electron is

$$(23) \quad r_g \approx 3 \times 10^8 \left(\frac{T}{10^8 \text{ K}} \right)^{1/2} \left(\frac{B}{1 \mu\text{G}} \right)^{-1} \text{ cm}.$$

These very small gyroradii probably insure that the ICM acts as a fluid even when the Coulomb mean free paths are long.

3.4. *Transport Processes.* – The fact that the mean free paths are small but finite implies that the local properties of the gas will be influenced by the properties of the surrounding gas through diffusive processes, also called transport processes. These include the thermal conduction of heat energy in non-isothermal gases, the viscous transport of momentum, and the diffusion and settling of heavy elements within the intracluster gas. I will concentrate on thermal conduction here; viscosity and diffusion are discussed in [1].

3.4.1. Thermal Conduction. In a plasma with a gradient in the electron temperature, heat is conducted down the temperature gradient. If the scale length of the temperature gradient $l_T \equiv T/|\vec{\nabla}T|$ is much longer than the mean free path of electrons, $l_T \gg \lambda_e$, then the heat flux is given by

$$(24) \quad \vec{Q} = -\kappa \vec{\nabla}T,$$

where the thermal conductivity for a hydrogen plasma is [21]

$$(25) \quad \begin{aligned} \kappa &= 1.31 n_e \lambda_e k \left(\frac{kT_e}{m_e} \right)^{1/2} \\ &\approx 4.6 \times 10^{13} \left(\frac{T_e}{10^8 \text{ K}} \right)^{5/2} \left(\frac{\ln \Lambda}{40} \right)^{-1} \text{ erg cm}^{-1} \text{ s}^{-1} \text{ K}^{-1}. \end{aligned}$$

Because of the inverse dependence on the particle mass, thermal conduction is primarily due to electrons. If the very weak dependence of $\ln \Lambda$ on density is ignored, then κ is independent of density but depends very strongly on temperature.

If heat conduction operates at this ‘‘Spitzer’’ rate, then the gas in the central regions of clusters is likely to be isothermal. In addition, heat conduction would be very important at and would tend to eliminate any large local temperature gradients, such as appear to occur in the cool core of clusters or near cold fronts (§ 6). On the other hand, the rate of thermal conduction along a thermal gradient perpendicular to the magnetic field is very low, as a result of the small gyroradii of electrons (eq. 23). Thus, transverse or tangled magnetic fields may be able to suppress thermal conduction in clusters, at least in some regions. The existence of very steep temperature gradients in cold fronts has been used to argue that heat conduction is suppressed by factors of $\gtrsim 10^2$ in these regions (§ 6.2).

3.5. Hydrodynamics. – In the fluid limit, the ICM can be characterized by the local values of the gas density ρ , the gas pressure P , the gas temperature T or internal energy, and the gas velocity \vec{v} . The gas pressure is determined by the ideal gas law

$$(26) \quad P = \frac{\rho k T}{\mu m_p},$$

where μ is the mean mass per particle in terms of the mass of a proton m_p . The dynamical equation for a single component fluid is [25]

$$(27) \quad \rho \frac{D\vec{v}}{Dt} + \vec{\nabla}P + \rho \vec{\nabla}\Phi = 0,$$

where Φ is the gravitational potential, and D/Dt is the Lagrangian derivative with respect to time. Equation (27) ignores non-gravitational forces, such as magnetic stresses or viscosity. The continuity equation (mass conservation) is [25]

$$(28) \quad \frac{\partial \rho}{\partial t} + \vec{\nabla} \cdot (\rho \vec{v}) = 0.$$

There is also an equation giving the variation in the energy in the fluid. However, it is simpler to give this equation in terms of the entropy in the gas, S . A useful quantity to consider is the specific entropy per particle in the gas, $s \equiv S/N$, where N is the total number of particles. To within additive constants, the specific entropy of an ideal gas is

$$(29) \quad s = \frac{3}{2} k \ln \left(\frac{P}{\rho^{5/3}} \right) = \frac{3}{2} k \ln \left(\frac{T}{\rho^{2/3}} \right).$$

To avoid the logarithmic character of the entropy, it is conventional to define an “entropy parameter” K as

$$(30) \quad K \equiv \frac{kT}{(n_e)^{2/3}}.$$

with units of keV cm². Thus, $s \propto \ln K$. Then, the equation for the change in the gas entropy can be written [25]

$$(31) \quad \frac{\rho}{\mu m_p} k \frac{Ds}{Dt} = \mathcal{H} - \mathcal{L},$$

where \mathcal{H} and \mathcal{L} are the rate of heating and cooling per unit volume in the gas. In the absence of irreversible processes like heating or cooling or shocks, the specific entropy of a parcel of gas is constant.

3.6. Hydrostatic Equilibrium. – Unless it is disturbed in some way, one would expect the gas in a cluster to relax into hydrostatic equilibrium on roughly the sound crossing time of the cluster,

$$(32) \quad t_s \equiv \frac{D}{c_s} \approx 6.6 \times 10^8 \text{ yr} \left(\frac{T}{10^8 \text{ K}} \right)^{-1/2} \left(\frac{D}{1 \text{ Mpc}} \right).$$

Here, D is the diameter of the cluster, and c_s is the sound speed. Since this time scale is shorter than the age of a typical cluster, which is a fraction of the Hubble time, the gas in many clusters should be close to hydrostatic equilibrium. Exceptions would include clusters which are undergoing or have recently undergone a major merger, and regions of a cluster where an AGN has injected energy recently.

In hydrostatic equilibrium, the pressure forces balance gravity:

$$(33) \quad \vec{\nabla} P = -\rho \vec{\nabla} \Phi, \quad \frac{1}{\rho} \frac{dP}{dr} = -\frac{GM(r)}{r^2},$$

where $M(r)$ is the total cluster mass within r , and the second form assumes spherical symmetry. Because eq. (33) gives a single relation for two gas properties (density and pressure), one must also specify the entropy distribution of the gas to determine its distribution.

3.6.1. Isothermal Models. A very simple model follows if the gas is assumed to be isothermal ($T = \text{constant}$); isothermality might result if thermal conduction were efficient in the cluster (§ 3.4.1). Then, the solution of the hydrostatic equation is

$$(34) \quad \ln \left[\frac{\rho(r)}{\rho_0} \right] = \frac{\mu m_p}{kT} [\Phi_0 - \Phi(r)] ,$$

where ρ_0 and Φ_0 are the central values of the the gas density and gravitational potential, respectively. Note that the gas density will generally go to a finite value as $r \rightarrow \infty$.

As discussed above (§ 2.1.1), numerical simulations and observations suggest that the dark matter distributions in clusters should have a power-law drop off at large radii, and a flatter power-law at small radii. One standard form is the NFW [14] density profile (eq. 1). If this distribution applies to the sum of all the matter in a cluster, then the potential is

$$(35) \quad \Phi(r) = \Phi_0 \frac{\ln \left(1 + \frac{r}{r_s} \right)}{\frac{r}{r_s}} ,$$

and the central potential is $\Phi_0 = -4\pi G \rho_s r_s^2$.

However, in the past the dark matter and/or galaxy distributions in clusters were modeled using a function with a constant density core (§ 2.2), such as the analytic King model (eq. 8, fig. 1). If this form is assumed for the total matter density in a cluster, or if it applies to the galaxy distribution, and the galaxies have an isotropic gaussian velocity distribution, then the resulting gas density distribution is the “beta model” [26]

$$(36) \quad \rho(r) = \rho_o \left[1 + \left(\frac{r}{r_c} \right)^2 \right]^{-3\beta/2} .$$

If the gas is isothermal, then this density distribution gives an X-ray surface brightness distribution of the form

$$(37) \quad I_X(r) = I_X^o \left[1 + \left(\frac{r}{r_c} \right)^2 \right]^{-3\beta+1/2} .$$

This beta-model provides a reasonable fit to the X-ray surface brightness in the outer regions of many cluster, with a typical value of $\beta \approx 2/3$. However, it does not fit the inner parts of cool core clusters.

3.6.2. Adiabatic or Polytropic Models. The temperature profiles in clusters of galaxies are generally more consistent with a gradual decline with radius at large radii, rather than isothermal gas [27]. A simple alternative would be if the gas in clusters was adiabatic (had a constant specific entropy); then the pressure and density would vary together as

$P \propto \rho^\gamma$ with $\gamma = 5/3$. Often, one also considers distributions with the same pressure-density relationship, but for values of γ in the range $1 \leq \gamma \leq 5/3$. We will refer to these distributions as “polytropic.” Then, the hydrostatic equation can be solved to give

$$(38) \quad \frac{T(r)}{T_0} = 1 + (\alpha - 1) \left[1 - \frac{\Phi(r)}{\Phi_0} \right],$$

$$(39) \quad \frac{\rho(r)}{\rho_0} = \left[\frac{T(r)}{T_0} \right]^{1/(\gamma-1)}.$$

Here, T_0 is the central temperature, and $\alpha \equiv T(\infty)/T_0$. The temperature profiles in the outer parts of clusters can generally be fit with intermediate values of $\gamma \sim 1.2\text{--}1.3$ [28].

3.6.3. Surface Brightness Deprojection. The gas distributions in clusters can be derived directly from observations of the X-ray surface brightness of the cluster, if the shape of the cluster is known and if the X-ray observations are sufficiently detailed and accurate. The X-ray surface brightness at a photon frequency ν and at a projected distance b from the center of a spherical cluster is

$$(40) \quad I_\nu(b) = \int_{b^2}^{\infty} \frac{\epsilon_\nu(r) dr^2}{\sqrt{r^2 - b^2}},$$

where ϵ_ν is the X-ray emissivity. This Abel integral can be inverted to give the emissivity as a function of radius,

$$(41) \quad \epsilon_\nu = -\frac{1}{2\pi r} \frac{d}{dr} \int_{r^2}^{\infty} \frac{I_\nu(b) db^2}{\sqrt{b^2 - r^2}}.$$

The emissivity ϵ_ν is proportional to the square of the density, and its spectral dependence is determined by the gas temperature and abundances (eqs. 18, 19, & 20). Thus, the radial dependence of the spectrum and intensity of X-rays can be de-projected to the the gas density $\rho(r)$, gas temperature $T(r)$, and abundances as a function of physical radius. The gas pressure is then given by the ideal gas law (eq. 26).

3.6.4. Cluster Masses. Once the gas density has been determined by either model fitting or de-projection, the gas mass can be derived simply as

$$(42) \quad M_{\text{gas}}(r) = 4\pi \int_0^r \rho(r') (r')^2 dr'.$$

Here, $M_{\text{gas}}(r)$ is the gas mass interior to the radius r .

The total gravitational mass can be derived from the condition of hydrostatic equilibrium (eq. 33), which can be written as

$$(43) \quad M(r) = -\frac{r^2}{G\rho(r)} \frac{dP}{dr},$$

where $M(r)$ is the total mass interior to r . This equation can also be written as

$$(44) \quad M(r) = -\frac{kT(r)r}{\mu m_p G} \left[\frac{d \ln \rho(r)}{d \ln r} + \frac{d \ln T(r)}{d \ln r} \right].$$

Optical observations of the galaxies can be used to estimate the total mass of galaxies interior to r , $M_{\text{gal}}(r)$. Any diffuse stellar light can be included in this; although these values can be difficult to determine, the stars and galaxies constitute only a small fraction of the mass, so this correction is not so important. Then, the mass of dark matter in the cluster (interior to r) is given by

$$(45) \quad M_{\text{DM}}(r) = M(r) - M_{\text{gas}}(r) - M_{\text{gal}}(r).$$

In typical clusters, the masses of stars and galaxies are much smaller than those of the hot gas, with $M_{\text{gal}} \approx 0.15 M_{\text{bary}}$ at large radii [29]. Thus, hot plasma is the dominant form of baryonic matter in clusters of galaxies. It appears that the same may be true on large scales throughout the present day Universe; it seems that most of the baryons in the Universe today are in hot, diffuse intergalactic gas (often called WHIM, or Warm Hot Intergalactic Medium), rather than stars and galaxies (e.g., [30]). In this sense, cluster represent the tip of the iceberg. With their very high densities, they are the one place it has been easy to detect the bulk of the baryons, which are in intergalactic gas.

The gas mass fraction $f_{\text{gas}}(r)$ and baryon fraction $f_{\text{bary}}(r)$ are then

$$(46) \quad f_{\text{gas}}(r) = \frac{M_{\text{gas}}(r)}{M(r)}, \quad f_{\text{bary}}(r) = \frac{M_{\text{gas}}(r) + M_{\text{gal}}(r)}{M(r)}.$$

The observations of most clusters show an increase in $f_{\text{gas}}(r)$ with radius r in the inner parts of clusters [31]. Thus, the gas is more broadly distributed than the dark matter in clusters. The gas fractions level out at radii which are $r \gtrsim 0.2 r_{\text{vir}}$. Rich clusters have gas fractions which average $\langle f_{\text{gas}}(r_{2500}) \rangle = 12\%$ at a radius where the mean interior density is 2500 times the critical density [31]. For typical clusters, $r_{2500} \approx 0.25 r_{\text{vir}}$. The total gas fraction within r_{vir} will be a bit larger than this. Thus, clusters appear to consist of about 2-3% stars and galaxies, $\sim 14\%$ hot gas, and $\sim 84\%$ dark matter. Although these are recent values, clusters of galaxies provided some of the earliest evidence that the mass in the Universe was predominantly dark matter.

Clusters of galaxies are very useful cosmological probes. Arguably, they are the largest objects in the Universe which are dynamically relaxed. On the other hand, they are probably the smallest objects which formed from a sufficiently large volume that they contain a fair sample of the material in the Universe. Thus, the ratio of baryons to dark matter in clusters should be close to the universal value. Numerical simulations do indicate that the baryon fraction in clusters is nearly the general value in the Universe; even at r_{2500} , f_{bary} is about 82% of the universal value [32].

When combined with the density of baryons inferred from Big Bang nucleosynthesis, the observed baryon fraction in clusters indicates that the total mass density in the

Universe is $\Omega_M \approx 0.3$ [33]. Thus, clusters have provided some of the earliest and strongest evidence that we live in a low density Universe, with too little matter to close the Universe and reverse the expansion of the Big Bang.

The measured values of f_{gas} and f_{bary} depend on the distance d to a cluster as $d^{3/2}$. On the other hand, if clusters are fair samples of the materials in the Universe, then f_{bary} should be independent of redshift or distance. Thus, a comparison of f_{bary} in low redshift and high redshift clusters provides a measure of the distance to the clusters which is independent of the redshift. Such measurements provide evidence that we live in an accelerating Universe, with an effective cosmological constant of $\Omega_\Lambda \approx 0.7$ [31]. This is in concordance with the results from WMAP [7] and supernova Type Ia observations at high redshifts.

3.7. Heating and Cooling of Intracluster Gas. –

3.7.1. Why Is the ICM So Hot?. When it was first observed in X-rays, one of the most surprising features about the intracluster gas was its very high temperature. Why is this gas so hot? In fact, this is one of the easiest aspects of the ICM to understand. At least in rich clusters, most of the heating is gravitational in origin. The basic idea is that clusters have huge masses, and very deep gravitational potential wells. Essentially, any means of introducing the gas into a cluster will cause it to move very rapidly, and collide with other gas, and be shocked. For example, if the gas fell into the cluster (either at the same time as the dark matter, or subsequently), cluster gravitational potentials imply that the gas would fall in at a speed $\gtrsim 1000 \text{ km s}^{-1}$. Unless the gas motions were very carefully controlled, the gas would encounter other gas moving at similar velocities, and the intersecting gas streams would collide and shock. Since the ICM has heavy elements, a portion of it came out of galaxies. If it did so after the clusters formed, then the galaxies would be moving at orbital speeds of $\gtrsim 1000 \text{ km s}^{-1}$ in the cluster, and gas ejected from different galaxies would collide and shock at these sorts of speeds. (If the gas came out of galaxies before clusters formed, then it had to fall into a cluster, and was shocked as described previously.) Thus, it is likely that essentially all of the gas in the ICM medium shocked at speeds of $\gtrsim 1000 \text{ km s}^{-1}$, and was heated in this way.

In actually, we believe that clusters form hierarchically from the merger of smaller groups and clusters. Such mergers are discussed extensively below (§ 5). Thus, the specific mechanism for much of the heating of the ICM is likely to be merger shocks.

3.7.2. Simple Scaling Laws for Gravitational Heating. If one assumes that gravitational heating dominates in clusters, and makes a few other simple assumptions, it is possible to derive a number of simple scaling laws for the X-ray properties of clusters [34]. If the gas in clusters is in hydrostatic equilibrium and is distributed similarly to the dark matter, then the typical gas temperature should be $kT \sim \mu m_p GM/R$, where M is the total cluster mass, and R is the cluster radius. If one can treat the formation of a cluster as equivalent to the collapse of a isolated, spherical region of overdensity in the Universe, then the post-collapse average density in the cluster should be $\langle \rho_{\text{tot}} \rangle \sim 180 \rho_{\text{crit}}(z_{\text{form}})$, where ρ_{tot} is the total mass density (dark matter and baryons), and $\rho_{\text{crit}}(z_{\text{form}})$ is the

critical density for the Universe to collapse at the epoch of formation of the cluster. If most clusters have formed recently, then one could approximate $z_{\text{form}} \sim 0$. Finally, clusters are large enough to contain a fair sample of the material in the Universe, and thus it is reasonable to assume that the baryon fraction in clusters (which is predominantly in the hot gas) is the universal value (§ 3.6.4). Then, the radii of clusters should scale with mass as

$$(47) \quad R \propto M^{1/3}.$$

The gas temperature would scale as

$$(48) \quad T \propto M^{2/3},$$

and the X-ray luminosity vs. temperature relationship would be

$$(49) \quad L_X \propto T^2.$$

The latter scaling assumes that the X-ray emission is mainly due to thermal bremsstrahlung, which is true for hot clusters.

3.7.3. Non-Gravitational Heating. There are a number of indications that non-gravitational heating or cooling processes may affect the ICM, particularly in smaller clusters and groups. First, the observed cluster X-ray properties do not agree very well with the scaling relations for purely gravitational heating (eqs. 47–49). Probably, the most significant deviation is that the measured X-ray luminosity–temperature relation is much steeper than eq. (49) [35]. The departures for the scaling relations are particularly strong for cooler clusters and groups. Second, the observed gas distributions in clusters are more extended than would be expected from purely gravitational heating. The gas distributions often have central cores. This suggests that some non-gravitational heating processes have occurred and have puffed up the gas distributions, particularly in the poorer clusters. This would lower the average density in the gas, and thus reduce the X-ray luminosity. An alternative possibility is that inhomogeneous cooling has removed the cooler ICM, increasing the average temperature of the gas which remains. Presumably, this cooling would also lead to star and galaxy formation. These topics have been reviewed extensively in [3].

If the non-gravitational heating occurred just prior to the collapse of a cluster, then the amount of heat needed is ~ 2 keV per particle [36]. However, a more useful quantity to describe the preheating is probably the extra entropy per particle Δs (eq. 29). As noted in § 3.5, the specific entropy is a Lagrangian quantity which moves with the gas, and which remains constant for reversible changes. As discussed in § 3.5, it is conventional to use the entropy parameter K (eq. 30) rather than s . For purely gravitational heating, the scaling laws described above (§ 3.7.2) imply that the entropy parameter is expected to scale as

$$(50) \quad K \propto T \propto M^{2/3}.$$

Observations of clusters and groups initially suggested that preheating produced an extra entropy of $\Delta K \approx 135 \text{ keV cm}^{-2}$ [37, 38]. It now appears that such an “entropy floor” may be too simplified an explanation for the detailed variations in entropy between clusters and the radial variations within clusters. Also, the existence of the Lyman alpha forest and other quasar absorption lines indicates that not all of the intergalactic gas underwent the same level of preheating. Nonetheless, this value provides a useful value in assessing models for the thermal history of the ICM.

The radial variation of the entropy in the ICM also appears to be inconsistent with purely gravitational heating. Gravitational heating models predict that the entropy vary roughly as $K \propto r^{1.1}$. The observed entropy profiles in clusters are much flatter in the center [39].

Supernovae could provide a significant source of heating of the ICM. These would include core collapse supernova associated with the deaths of massive stars. Since the galaxies in clusters today contain very few such stars, this would have occurred during the epoch of star formation and galaxy formation. The supernovae might have driven galactic winds. The second type of supernovae are Type Ia’s, which are produced by older binary star systems. They would provide a more continuous source of heating.

Supernovae also eject heavy elements. Thus, the abundances in clusters can be used to limit the total number of supernova which have occurred. The observed abundances suggest that the extra energy added is probably $\sim 0.3 \text{ keV}$ per particle [36]. This is a bit low to explain the required preheating, but might be possible. However, this mechanism would also require that a large fraction of the supernova explosion energy be converted into heat in the ICM, which may also be a difficulty.

Active galactic nuclei (AGNs) within clusters might also provide a significant amount of heating. As with the supernovae, it is difficult to determine what fraction of the energy produced by AGNs goes into heating the surrounding medium. In this regard, it is only the AGN output in kinetic energy in jets or in relativistic particles which is likely to be useful. It may be important that the early-type galaxies found in clusters generally host radio galaxies and radio quasars, which are more likely to deposit energy into the ICM.

One way to limit the total energy input by AGNs is to look at the total masses of supermassive black holes contained in clusters today. In general, all large bulges appear to contain supermassive black holes, and there is a strong correlation of black hole mass with bulge mass or velocity dispersion. If the growth of black holes occurred largely by accretion (rather than merging of existing massive black holes), then the total accretion energy from black holes can be derived from their total mass. This could provide a significant level of heating for the ICM if the fraction of accreted energy which goes into heating is $\gtrsim 10\%$ [40].

3.7.4. Cooling in the Intracluster Medium. The primary cooling process for the ICM is the emission of X-ray radiation. The emission is proportional to the square of the density and varies with temperature (eqs. 18, 19, & 20). Thus, the total cooling rate per

unit volume \mathcal{L} in the gas can

$$(51) \quad \mathcal{L} = \Lambda(T, \text{Abundances}) n_e n_p,$$

where Λ depends only on the temperature and the abundances of the heavier elements relative to hydrogen. At high temperature ($kT \gtrsim 2$ keV), the dominant radiation is thermal bremsstrahlung, and $\Lambda \propto T^{1/2}$. At lower temperature, line emission becomes dominant, and Λ decreases with increasing temperature.

At high temperatures where thermal bremsstrahlung dominates, the time required for gas to cool to low temperatures at constant pressure is

$$(52) \quad t_{\text{cool}} = 69 \left(\frac{n_e}{10^{-3} \text{ cm}^{-3}} \right)^{-1} \left(\frac{T}{10^8 \text{ K}} \right)^{1/2} \text{ Gyr}.$$

Note that cooling accelerates as the gas cools; this tendency is even stronger below $kT \lesssim 2$ keV due to line emission. The cooling time is much longer than the Hubble time in the outer parts of clusters. However, it can be quite short ($t_{\text{cool}} \sim 300$ Myr) in the inner regions of cooling core clusters.

It is interesting to write the cooling time as a function of the entropy and temperature rather than the density and temperature:

$$(53) \quad t_{\text{cool}} = 17 \left(\frac{K}{130 \text{ keV cm}^{-2}} \right)^{3/2} \left(\frac{kT}{2 \text{ keV}} \right)^{-1} \text{ Gyr}.$$

Note that the cooling time is less than the Hubble time for $K \lesssim 130$ keV cm⁻² for $kT \sim 2.5$ keV. If clusters start with gas with a wide range of entropies, the lower entropy gas will cool rapidly and be removed from the ICM. Thus, cooling can increase the average entropy of the gas and provide an effective “floor” to the ICM entropy [41]. The cooled gas presumably goes into forming galaxies and stars. Feedback heating from supernovae, galactic winds, and AGNs (§ 3.7.3) might result in some of the cooled gas actually becoming hotter ICM. However, the result is to remove the cooler gas and raise the average entropy of the ICM.

Thus, while the bulk of the heating of the ICM in large clusters is due to gravitational heating, mainly by merger shocks, smaller clusters and the centers of clusters show evidence for the effects of non-gravitational heating and cooling. The cooling leads to star and galaxy formation, and which leads to possible heating by supernovae, galactic winds, and AGNs. Thus, the ICM (and intergalactic medium more generally) preserves a unique record of the thermal history of the Universe.

4. – Cool Cores in Clusters

A significant fraction of clusters of galaxies have cool, dense regions of intracluster gas at their centers. In this section, some of the basic properties of the “cool cores” are discussed.

4.1. *Basic Properties of Cool Cores.* – Early observations of cooling core clusters established a number of basic X-ray properties. First, these clusters had very bright central peaks in their X-ray surface brightness. Second, X-ray spectra indicated that the gas had a positive radial temperature gradient; the gas got cooler as the radius decreased within the cooling core. Third, the observed gas densities and temperatures implied that the radiative cooling time of the gas was less than the Hubble time within the cooling cores. In the densest regions in the centers of cooling core clusters, the radiative cooling times typically drop to values of $t_{\text{cool}} \sim 2 \times 10^8$ yr. These properties were found in a significant fraction of clusters, generally at least 50%. (For reviews of the early properties of cooling cores, see [42, 2].)

4.2. *Simple Cooling Flow Model.* – These observational properties led to a simple theoretical model for cooling flows. The basic assumption was that the energy in the X-rays which we see comes from the thermal energy content of the ICM. A second assumption was that no heating process balances this radiative cooling; this is the idea which now appears to be wrong in detail. Third, it is assumed that the gas at the centers of clusters is not disrupted or disturbed or mixed into the outer ICM. If this is the case, then the gas will cool radiatively. The weight of the surrounding cluster gas will compress the cooling central gas, and it will flow slowing (subsonically) toward the center of the cluster. This will result in denser, cooling gas at the center of the cluster, in agreement with the observations. If no heating process balances the cooling, the gas should cool down to very low temperature, certainly below the X-ray emitting range. If the gas cools nearly isobarically and if the energy input from inflow in the gravitational potential is small, then the total cooling luminosity would be

$$(54) \quad L_{\text{cool}} \approx \frac{5}{2} \frac{kT}{\mu m_p} \dot{M},$$

where T is the initial temperature of the cooling gas, \dot{M} is the cooling rate (mass per unit time), and μm_p is the mean mass per particle in the gas. Applying this equation to the X-ray surface brightnesses of cooling cores in clusters led to estimated cooling rates of $\dot{M} \gtrsim 100 M_{\odot}/\text{yr}$ in many clusters.

If one assumes that the gas in the cooling flow achieves steady-state, is spherically symmetric, and is homogeneous, and that there is no nongravitational heating, the hydrodynamical equations (eqs. 27, 28, & 31) take a simpler form. The continuity (mass conservation) equation becomes (eq. 28)

$$(55) \quad \frac{1}{r^2} \frac{d}{dr} (r^2 \rho v) = 0,$$

which implies that the inflow rate

$$(56) \quad \dot{M} \equiv -4\pi\rho v r^2 = \text{constant}.$$

Euler's equation (eq. 27) becomes

$$(57) \quad \rho v \frac{dv}{dr} + \frac{dP}{dr} + \rho \frac{d\phi(r)}{dr} = 0,$$

and the energy/entropy equation becomes

$$(58) \quad \frac{1}{r^2} \frac{d}{dr} \left\{ r^2 \rho v \left[\frac{v^2}{2} + \frac{5}{2} \frac{P}{\rho} + \phi(r) \right] \right\} = -\mathcal{L}.$$

In general, the cooling times (eq. 52) are longer than the sound crossing times (eq. 32) for the cool cores in clusters. This implies that the motions in any cooling flow are highly subsonic, $v^2 \ll c_s^2$. If the changes in gravitational potential $\phi(r)$ within the cool core are smaller than the thermal energy per unit mass of the gas, then the potential $\phi(r)$ makes a small contribution in eqs. (57) and (58), and the pressure is nearly constant in the cool core, $P \approx \text{constant}$. Integrating eq. (58) over the volume of the cool core then gives the eq. (54) for the luminosity. If the cooling is mainly due to thermal bremsstrahlung (eq. 18) with $\mathcal{L} \propto \rho^2 T^{1/2}$, then the solution to eqs. (58), (57), and (55) for an isobaric, subsonic flow is $T \propto r^{6/5}$ and $\rho \propto r^{-6/5}$ [43]. This gives a bolometric X-ray surface brightness which varies as $I_X \propto r^{-4/5} \sim 1/r$ and an interior bolometric X-ray luminosity which varies as $L_X(r) \propto r^{6/5} \sim r$.

4.3. Early Results in Other Wavebands. – Early optical observations established that cluster cool cores were always centered on a large, cluster-dominant elliptical galaxy. These ellipticals were unusual in having extensive systems of optical emission line filaments from gas at $\sim 10^4$ K (e.g., [44, 45, 46, 47]). The central elliptical galaxies in cooling cores also were found to have very blue colors, which indicated that they contained relatively young stars (e.g., [48, 49, 50]). The emission lines and young stars appeared to be correlated with structures in the X-ray and radio images of the same systems (e.g., [51]).

Many cooling core clusters also have dust, and cooler gas observed through IR emission, 21 cm emission and absorption, and CO emission (e.g., [52]).

4.4. The Cooling Flow Problem: Reservoir for the Cooling Gas? – Initially, it was thought that these cooler forms of gas or star formation might represent the ultimate reservoir of the hot gas which was seen to cool through part of the X-ray band. Unless the gas is reheated in some way, radiative cooling should accelerate as the temperature drops. Thus, one might expect the gas to cool down to low temperatures, and form stars. The discovery of significant amounts of cooler gas and of young stars in cooling core ellipticals appeared to be qualitatively consistent with this expectation. Unfortunately, this result did not work quantitatively. The amounts of cool gas were generally much smaller than the estimates of the cooling rates integrated over a significant fraction of the Hubble time. Similarly, the present star formation rates are much lower than the early estimates of the cooling rates. It appeared that a few percent of the cooling gas could be consumed by star formation or stored as cold gas in the observed forms, but not the full expected

amount. This discrepancy became known as the “cooling flow problem”: where does most of the cooling gas go?

4.5. XMM-Newton and Chandra Results: High Resolution Spectra. – The RGS gratings on XMM-Newton (and, to a lesser extent, the gratings on Chandra) have provided high resolution X-ray spectra of a sample of cooling core clusters. In this regard, the low energy grating spectra are particularly important. In the standard cooling flow model without reheating, all of the gas which cools from higher temperatures should continue to cool out of the X-ray band. As the gas cools below 10^7 K, heavy elements will recombine and produce very strong line emission. One particularly strong set of lines produced at lower temperature come from Fe XVII (or Fe⁺¹⁶); these lines mainly lie below 1 keV in the spectrum. The XMM-Newton spectra showed that Fe XVII and other low ionization lines were missing from the spectra of cluster cooling cores at the level predicted by the standard cooling flow model without reheating (e.g., [53]), and this result was confirmed with Chandra.

In detail, the high resolution spectra showed that most of the gas in cluster cooling cores only cools down to $\sim 1/2$ or $1/3$ of its initial temperature [53]. If the emission measure is modeled as a power-law function of the temperature, the luminosity emitted in each temperature range is found to vary as $dL_X/dT \propto T^{1-2}$, rather than $dL_X/dT \propto T^0$ as predicted by the standard cooling flow model without reheating (eq. 54). Thus, there is much less emission at low temperatures than expected in this model. The upper limits on the cooling rate to low temperatures (and a few possible detections of low temperature X-ray emission) are all roughly consistent with only 1–10% of the gas cooling at high temperatures continuing to low temperatures. These results appear to resolve at least one version of the standard cooling flow problem; the quantities of gas cooling to low temperatures are now consistent with the amounts of cool gas and rates of star formation observed in these systems (§§ 4.3, 4.4).

On the other hand, it is likely that some heating process is required to explain the small amounts of gas which continue to cool to low temperatures. In fact, the heating cannot merely balance cooling, which would cause the gas to accumulate at $\sim 1/3$ of its original temperature; gas which has cooled must be reheated back to nearly the ambient temperature. Although very inhomogeneous abundances [54] or nonradiative cooling (e.g., [55, 56]) may also play a role, it is likely that some heating process accounts for most the deficit of low ionization X-ray lines.

Another important result is that the high resolution spectra do not show evidence for large amounts of local X-ray absorption in cooling cores [53], as had been suggested based on previous lower resolution spectra (e.g., [57]).

The existing high resolution spectra of cooling cores mainly give upper limits to the rate of cooling to very low temperatures. Since some cooler gas and star formation are seen in these systems, it is likely that some gas is cooling to very low temperatures, at least part of the time. As noted above, the existing limits are generally consistent with the amounts of cool gas and star formation. It would be very useful to improve the spectral measurements to either give measured values for the cooling rate to low

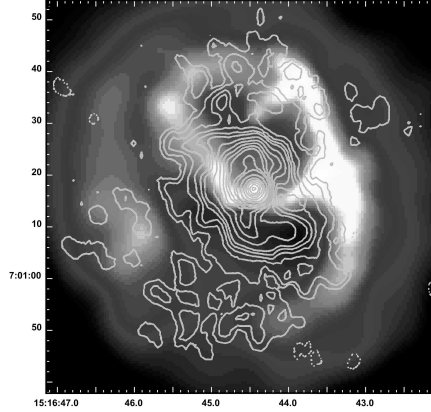


Fig. 5. – Chandra X-ray image (greyscale) of the center of Abell 2052, with radio contours superposed [58, 59]. There are holes in the X-ray image surrounded by bright shells. The radio emission fills the holes.

temperatures, or to give upper limits which were inconsistent with the measurements of cooler materials.

4.6. Heating Source for Cooling Gas? – As noted above, the most likely explanation of the relative scarcity of cool gas and star formation in cool cores is that the radiatively cooling gas is heated by some process, which prevents most of the gas from cooling to low temperatures. In general terms, there are a large number of candidates for this heat source. One possible heat source is the vast thermal reservoir of the ICM in the outer parts of the cluster. The cooling gas might be reheated by thermal conduction from this outer gas (§ 3.4.1). As was noted in § 3.4.1, thermal conduction might be suppressed by tangled magnetic fields in clusters. If it is not suppressed, conduction could play an important role in heating the outer parts of cool cores. However, it is more difficult to understand how it can stop the cooling of the densest, coolest X-ray gas near the centers of cool cores. Since thermal conduction is most effective for very hot gas (the heat flux varies roughly as $Q \propto T^{7/2}$), it can more easily heat the hotter outer cool core gas than the cooler, denser gas near the center. Other heating mechanisms are discussed in § 3.7.3. Supernova could play a role, but the rate seems too low to account for the bulk of the heating. Cluster dynamics (mergers, sloshing, etc.) might provide some heating, but it is difficult to understand how they would generally suppress cooling. The leading candidate is heating by central AGNs, specifically radio galaxies.

4.7. Early Radio Results on Cool Cores. – In a very high proportion ($\gtrsim 70\%$) of cool core clusters, the central galaxy is a moderately bright radio source (e.g., [60]), and this proportion is much higher than for other elliptical galaxies. These radio galaxies are typically FR I sources, with small, spatially distorted structures. The extended portions often have rather steep radio spectra, which is consistent with their being confined by the

gas X-ray emitting gas. Many of the brightest, nearby radio galaxies are at the centers of cooling core clusters (e.g., Virgo A, Perseus A, Hydra A, Cygnus A, etc.)

In general, the radio lobes of these cooling core radio sources are strongly polarized, but have extremely large Faraday rotations (e.g., [61]), indicating that there are very strong magnetic fields in cooling cores [62].

4.8. Radio Bubbles. – As noted in § 4.7, in almost all cases the central galaxies in cooling cores are radio sources. Chandra and XMM-Newton observations have provided dramatic evidence for the interaction of these radio sources with the intracluster gas. For example, fig. 5 shows the Chandra X-ray image (greyscale) of Abell 2052, with radio contours superposed [58]. In the X-ray, these radio bubbles generally show two holes in the X-ray surface brightness on opposite sides of the galaxy nucleus. In most cases, the holes are surrounded by bright shells of X-ray emission. The X-ray holes correspond to the lobes of the central radio source. For the systems with a relatively simple geometry, deprojection analysis indicates that the X-ray surface brightness in the holes is consistent with foreground and background cluster emission; that is, the holes appear to be empty of X-ray emitting gas. The masses of X-ray gas in the surrounding shells are consistent with the mass which is missing from the holes [59]. All of this is consistent with a picture in which the central radio source has sent out two jets, which have been stopped in the cooling core gas. The jets have inflated two lobes, and the radio plasma has displaced the X-ray gas and compressed it into the two surrounding shells. In a few cases, similar radio bubbles were seen originally with ROSAT [63, 64, 65, 66]. The most spectacular case, in terms of the detail of the observations, is the Perseus cluster, where there is a very long Chandra exposure [67]. The properties of radio bubbles are reviewed in [4].

In many cooling core clusters, “ghost bubbles” are also seen at larger radii from the center. These are holes in the X-ray emission without associated high frequency radio emission. Figure 6 shows Abell 2597, an example of a cooling core with ghost bubbles [68]. Recently, low frequency radio images have detected radio emission in many of the ghost bubbles (e.g., [69]). In general, the properties of the ghost bubbles are consistent with older radio bubbles which have risen buoyantly in the cluster atmosphere.

Although the radio bubbles show an anticorrelation between radio and X-ray emission, in a few systems there is evidence for a form of positive correlation. Specifically, columns of cool, dense gas are seen going from the center of the central galaxy out to the radio lobes. Examples include Virgo/M87 [70] and Abell 133 [71] (fig. 7). One suggestion is that these X-ray features are due to cooler gas from the center of the cooling core which has been entrained and uplifted by a buoyant radio lobe.

X-ray spectral observations show that the X-ray bright shells around radio bubbles are generally cool, and that the pressures in these shells are similar to those of the surrounding hotter gas. This indicates that these shells are not due to shocks, and that the radio sources are not expanding very supersonically. However, recently a few clusters have been found in which the radio lobes are surrounded by shells of hot gas, indicating that the radio sources are driving moderately strong shocks. Examples include MS0735.6+7421 [72], which is shown in fig. 8, Hydra A [73], and Herc A [74].

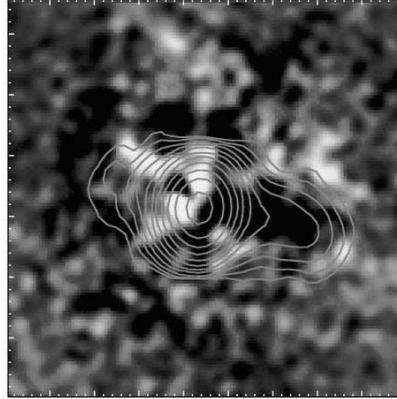


Fig. 6. – Greyscale is the Chandra residual image of Abell 2597 after subtraction of an elliptical model, with low frequency (330 MHz) radio contours superposed [69]. The low frequency radio emission extends out into the “ghost bubble” to the west; also, there may be a channel in the X-ray image connecting the ghost bubble with the AGN at the center.

For the majority of the bubbles which are expanding subsonically or mildly transonically, the pressure within the bubbles must be comparable to the pressure in the X-ray gas external to the bubbles. For the sources with supersonic expansion, the internal pressures must be even higher. However, when the pressures in the radio lobes are estimated by the standard minimum energy or equipartition arguments, they are found to be ~ 20 times smaller than required in most cases (e.g., [59]). This indicates that we have not identified the primary energy content and pressure source within radio sources. It may be that the magnetic fields are larger than given by equipartition. The extra pressure might be due to a large population of low energy relativistic electrons, or to a very large population of relativistic ions. Alternatively, the radio sources may contain diffuse but very hot thermal gas, which provides most of the energy and pressure. Within the radio sources, jet kinetic energy is dissipated by shocks or other frictive processes, so it would not be surprising in most of the energy was thermalized. So far, it has been difficult to detect such hot gas in X-ray spectra of the radio lobes (e.g., [59]). However, it should be detectable with high spatial resolution SZ images [75].

4.9. X-ray Shells as Radio Source Calorimeters. – Radio bubbles are very useful systems for determining the total energies supplied by the jets in the radio sources. For the systems which are expanding subsonically, the total energy is the “PdV” work done to displace the X-ray emitting gas, plus the internal energy in the radio bubble [76]. (For systems with shocks, the shock energy needs to be included [72].) This gives a total energy of

$$(59) \quad E_{\text{radio}} = PV + \frac{PV}{\gamma - 1} = \frac{\gamma}{\gamma - 1} PV = (2.5 - 4) PV,$$

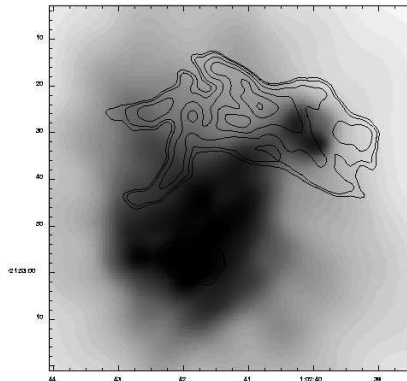


Fig. 7. – Chandra X-ray image (greyscale) of the center of Abell 133, with radio contours superposed [71]. There is a column of cool, dense, X-ray bright gas extending from the nucleus (at the lower left) to the extended radio source (upper right).

where P is the pressure in the radio lobe, V is its volume, and γ is the mean adiabatic index of the contents of the radio lobe. The two terms in the left end of the equation are the work done by the bubble and its internal energy. The range of values at the right of the equation correspond to the range from non-relativistic gas ($\gamma = 5/3$) to relativistic material ($\gamma = 4/3$). For example, in Abell 2052 the total energy is $E_{\text{radio}} \approx 10^{59}$ ergs [59], which is a typical value. Similar measurements have provided the best direct evidence on the total energy content of radio jets.

4.10. Can Radio Sources Offset Cooling?. – The energy in the radio source can be compared to the cooling X-ray luminosity of the cooling core to see if it is energetically possible for the radio source to inhibit the radiative cooling of the gas. To make this comparison, one needs a time scale for the activity of the radio source; typically, this is given by the buoyancy rise time of the radio bubbles. In most cases, this comparison indicates that energy from the radio source could balance radiative cooling (e.g., [77]), although this is not true in all cases. Radio heating (as well as the common occurrence of radio sources in cooling cores) requires that the radio activity be episodic; it may be that the average radio power is more important than the current value.

In general, AGNs have a very large range in their luminosities, which presumably reflects, at least in part, a large range in their energy output. Thus, it would seem unlikely that heating by radio sources would balance radiative cooling by X-ray gas in cluster cool core in every case without some sort of “feedback” between the AGN activity and the cooling of the gas. If the AGN is powered by the accretion of cooled X-ray gas, such a feedback loop seems possible. For example, consider a cluster containing a BCG with a supermassive black hole at its center. Assume the cluster formed recently or underwent a major merger, and that there is initially no gas which has cooled at the center of the cluster. Thus, the cluster would lack a cool core, and the AGN would be inactive due to a lack of material to accrete. Eventually, radiative cooling would lead

some gas to cool at the center of the cluster where the density is highest, and thus the cooling time is shortest (eq. 52). This would lead to gas cooling at the center of the cluster, and some small fraction of this gas would reach the central supermassive black hole and be accreted. The AGN would become active, and would launch jets into the surrounding cluster cool core. Assume that these jets are stopped in the cool core and heat the gas there, suppressing cooling. This would stop the cooling, and eventually starve the AGN of fuel. This might either lead to a stable balance in which just enough gas cooled to low temperatures to power the AGN sufficiently to heat the cool core gas enough to prevent further cooling. Perhaps more likely, this would lead to an episodic limit cycle, with periods of cooling and AGN activity, and the average heating rate by the AGN nearly balancing the average cooling rate by the X-ray gas

4.11. AGN Feedback and Massive Galaxy Formation. – Similar processes of AGN feedback may have played a very important role in the formation of galaxies, particularly massive galaxies. In principle, AGN feedback can solve a major problem with galaxy formation. In the absence of any feedback, one might expect that every large dark matter halo would contain gas which formed stars, and thus each large halo would become a galaxy. In fact, there are fewer massive galaxies than would be expected from the number of massive dark matter halos [78]. Simple prescriptions for AGN feedback in galaxy formation can reduce the luminosity function of massive galaxies to the approximate levels observed (e.g., [78]). Thus, AGN feedback is likely to have been very important during galaxy formation at high redshifts.

Cluster cool cores with radio bubbles provide wonderful local “laboratories” for studying radio mode AGN feedback and the suppression of gas cooling and star formation. Due to the low redshifts of the nearby local clusters, the physics of these processes can be studied in much more detail than is possible for high redshift, newly forming galaxies.

4.12. Radio Source Heating Mechanism in Cool Cores. – Although the radio sources in the centers of cluster cool cores have enough energy, in most cases, to suppress cooling (§ 4.10), the detailed mechanism by which they heat the gas is still poorly understood. How can one get heat preferentially into the cooler gas? How is the heat transported to the outer parts of the cool core without disrupting (e.g., by convection) the cool core and the observed abundance gradients there? It may be that the radio plasma mixes with the X-ray plasma, or that relativistic particles diffuse into the thermal gas, and directly heat the gas. The X-ray gas might be heated by plasma waves, sound waves, or weak shocks generated by the radio source. The deep Chandra image of the center of the Perseus cluster shows ripples which are probably sound waves and weak shocks from the radio source [67]. The problem of heating is complicated by the fact that the energy is initially in the directed flow of the radio jets. How do initially narrow radio jets heat the X-ray gas in all directions (e.g., [79])? Why don’t the jets just punch narrow channels in the gas? Is the collimated outflow disrupted by jet precession, or cluster gas motions, or instabilities? Does most of the energy actually come out in wider jets or winds? The detailed nature of the AGN heating and feedback in cool cores is a very active area of

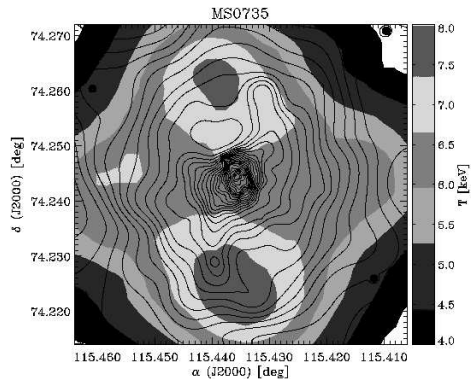


Fig. 8. – Greyscale is the Chandra temperature map of the center of the cluster MS0735.6+7421, while the contours are the X-ray surface brightness [72]. The radio bubbles in this cluster are bounded by hot regions, which indicates that the radio source is driving shocks into the intracluster gas.

research.

5. – Cluster Mergers

Major cluster mergers are the most energetic events in the Universe since the Big Bang. Cluster mergers are the mechanism by which clusters are assembled. In major mergers, the subclusters collide at velocities of ~ 2000 km/s, releasing gravitational binding energies of as much as $\gtrsim 10^{64}$ ergs. During mergers, shocks are driven into the intracluster medium. In major mergers, these hydrodynamical shocks dissipate energies of $\gtrsim 10^{63}$ ergs; such shocks are the major heating source for the X-ray emitting intracluster medium. The shock velocities in merger shocks are similar to those in supernova remnants in our Galaxy, and we expect them to produce similar effects. Mergers shocks heat and compress the X-ray emitting intracluster gas, and increase its entropy. We also expect that particle acceleration by these shocks will produce relativistic electrons and ions, and these can produce synchrotron radio, inverse Compton (IC) EUV and hard X-ray, and gamma-ray emission. (See the chapter by Rephaeli for more details on relativistic particles and nonthermal emission in clusters.)

5.1. Cluster Formation and Large Scale Structure. – Clusters of galaxies form hierarchically, with smaller systems (galaxies, groups of galaxies, and small clusters) forming first. Gravity pulls these smaller systems together, and they merge to form larger clusters. Since they are rare, extremely dense regions, clusters form in the densest regions of the Universe. Numerical simulations of large scale structure (LSS) show that these regions form a filamentary structure in the Universe, and clusters form within these LSS filaments, often at the intersections of filaments. Clusters are forming by mergers today, and have formed over much of the history of the Universe.

Cluster form by a combination of large and small mergers; see the merger tree in fig. 2 for an example of this. Often, the bigger merger events are referred to as “major mergers”, while the more continuous effect of smaller mergers is referred to as “accretion.”

5.2. Accretion Shocks. – One simple limit for the process of accretion would be a single cluster forming in an otherwise uniform cold Universe. For a spherical cluster forming in a uniform, Einstein-deSitter universe, there are self-similar solutions for both the dynamics of collisionless components (the galaxies and the dark matter) and for the accretion of cold gas [80]. Neither the dark matter nor the gas distributions within these self-similar solutions agree very well with the observed distributions in real clusters, or with the results from three dimensional LSS simulations. The main feature of the hydrodynamical solutions for the spherical accretion of gas is a spherical accretion shock. Since the accreted gas in the self-similar solutions is cold, this is a very strong shock. It is expected to occur at large radii (~ 2 Mpc), somewhat beyond the virial radius of the cluster.

In hydrodynamical simulations of the growth of clusters within LSS, the geometry of the resulting shocks is much more complex [81, 82]. Rather than continuous, spherically symmetric accretion, gas is added in episodic merger events occurring primarily along the LSS filaments. There are accretion shocks surrounding the filaments, more localized accretion shocks along the filaments, and internal shocks due to mergers within the clusters. The accretion shocks within these simulations are strong, with Mach numbers $\mathcal{M} \equiv v_s/c_s \sim 30$. Here, v_s is the shock velocity relative to the pre-shock accreting gas, and c_s is the sound speed in the pre-shock gas. The accretion shocks generally are located at large radii of several Mpc from the cluster centers. The outermost accretion shocks tend to have a “tubular” geometry, surrounding the LSS filaments.

As far as I am aware, there have been no clear direct detections of accretion shocks around clusters up to the time this chapter was written. The accretion shocks occur at large radii in very low density regions. Since the X-ray emissivity increases with the square of the gas density (§ 3.2), the X-ray surface brightnesses of accretion shocks are expected to be quite low. It is possible that they will eventually be detected with SZ images, which measure the pressure column in the gas, and are thus sensitive to density rather than its square. In some cases, the presence of diffuse radio relics at large radii from clusters may be providing indirect evidence for accretion shocks.

One overall result of accretion shocks in LSS is that most of the baryons in the present day Universe should have passed through such shocks (mainly due to smaller systems than clusters). This leads to the prediction that most of the baryons in the present day Universe are in a warm or hot intergalactic medium (WHIM).

5.3. Thermal Physics of Merger Shocks. – The intracluster medium (ICM) is generally close to hydrostatic equilibrium in clusters which are not undergoing strong mergers. The virial theorem then implies that the square of the thermal velocity (sound speed) of the ICM is comparable to the gravitational potential. During a merger, the infall velocities of the subclusters are comparable to the escape velocity, which implies that the square of the

infall velocity is larger (by roughly a factor of two) than the gravitational potential. Thus, the motions in cluster mergers are expected to be supersonic, but only moderately so. As a result, one expects that cluster mergers will drive shock waves into the intracluster gas of the two subclusters. Let v_s be the velocity of such a shock wave relative to the preshock intracluster gas. The sound speed in the preshock gas is $c_s = \sqrt{(5/3)P/\rho}$, where P is the gas pressure and ρ is the density. Then, the Mach number of the shock is $\mathcal{M} \equiv v_s/c_s$. Based on the simple argument given above, one expects shocks with Mach numbers of $\mathcal{M} \lesssim 2$. Stronger shocks may occur under some circumstances, such as in the outer parts of clusters, or in low mass subclusters merging with more massive clusters.

Shocks are irreversible changes to the gas in clusters, and thus increase the entropy S in the gas. A useful quantity to consider is the specific entropy per particle in the gas, s (eq. 29). Observations of X-ray spectra can be used to determine T , while the X-ray surface brightness depends on ρ^2 . Thus, one can use X-ray observations to determine the specific entropy in the gas just before and just after apparent merger shocks seen in the X-ray images. Since merger shocks should produce compression, heating, pressure increases, and entropy increases, the corresponding increase in all of these quantities (particularly the entropy) can be used to check that discontinuities are really shocks (e.g., not “cold fronts” or other contact discontinuities, § 6.2).

In [22], this test was applied to ASCA temperature maps and ROSAT images of Cygnus-A and Abell 3667, two clusters which appeared to show strong merger shocks. Recent Chandra images have shown that the feature in Abell 3667 is a cold front [83]. In Cygnus-A, the increase in specific entropy in the shocked regions is roughly $\Delta s \approx (3/2)k$. The specific heat per particle q which must be dissipated to produce this change in entropy is $q \approx T\Delta s \approx (3/2)kT$, or about the present specific heat content in the shocked gas. Thus, these observations provide a direct confirmation that merger shocks contribute significantly to the heating of the intracluster gas.

The most dramatic merger shock which has been seen with Chandra is in the “Bullet Cluster” 1E0657–56 [11, 12, 13]. This is a very high velocity (~ 4500 km s⁻¹) merger occurring nearly in the plane of the sky, with a merger bow shock located ahead of a “cold front” (§ 6.2). Another prominent merger shock with a Mach number of $\mathcal{M} \approx 2.1$ is seen in Abell 520 [84]. In both cases, the merger shocks appear to have associated diffuse radio emission.

5.4. Shock Kinematics. – The variation in the hydrodynamical variables in the intracluster medium across a merger shock are determined by the standard Rankine–Hugoniot jump conditions [25], if one assumes that all of the dissipated shock energy is thermalized. Consider a small element of the surface of a shock (much smaller than the radius of curvature of the shock, for example). The tangential component of the velocity is continuous at the shock, so it is useful to go to a frame which is moving with that element of the shock surface, and which has a tangential velocity which is equal to that of the gas on either side of the shock. In this frame, the element of the shock surface is stationary, and the gas has no tangential motion. Let the subscripts 1 and 2 denote the preshock and post-shock gas; thus, $v_1 = v_s$ is the longitudinal velocity of material into

the shock (or alternative, the speed with which the shock is advancing into the preshock gas). Conservation of mass, momentum, and energy then implies the following jump conditions

$$(60) \quad \begin{aligned} \rho_1 v_1 &= \rho_2 v_2, \\ P_1 + \rho_1 v_1^2 &= P_2 + \rho_2 v_2^2, \\ w_1 + \frac{1}{2} v_1^2 &= w_2 + \frac{1}{2} v_2^2. \end{aligned}$$

Here, $w = P/\rho + \epsilon$ is the enthalpy per unit mass in the gas, and ϵ is the internal energy per unit mass. If the gas behaves as a perfect fluid on each side of the shock, the internal energy per unit mass is given by

$$(61) \quad \epsilon = \frac{1}{\gamma - 1} \frac{P}{\rho},$$

where γ is the ratio of specific heats (the adiabatic index) and is $\gamma = 5/3$ for a fully ionized plasma. The jump conditions can be rewritten as:

$$(62) \quad \begin{aligned} \frac{P_2}{P_1} &= \frac{2\gamma}{\gamma + 1} \mathcal{M}^2 - \frac{\gamma - 1}{\gamma + 1} = \frac{5}{4} \mathcal{M}^2 - \frac{1}{4} \\ \frac{v_2}{v_1} = \frac{\rho_1}{\rho_2} \equiv \frac{1}{C} &= \frac{2}{\gamma + 1} \frac{1}{\mathcal{M}^2} + \frac{\gamma - 1}{\gamma + 1} = \frac{3}{4} \frac{1}{\mathcal{M}^2} + \frac{1}{4}, \end{aligned}$$

where $C \equiv \rho_2/\rho_1$ is the shock compression, and the far right hand side assumes $\gamma = 5/3$.

If one knew the velocity structure of the gas in a merging cluster, one could use these jump condition to derive the temperature, pressure, and density jumps in the gas. At present, the best X-ray spectra for extended regions in clusters of galaxies have come from CCD detectors on ASCA, Chandra, XMM/Newton, and Suzaku. CCDs have a spectral resolution of >100 eV at the Fe K line at 7 keV, which translates into a velocity resolution of >4000 km/s. Thus, this resolution is (at best) marginally insufficient to measure merger gas velocities in clusters. In a few cases with very bright regions and simple geometries, the grating spectrometers on Chandra and especially XMM/Newton may be useful.

At present, X-ray observations can be used to directly measure the temperature and density jumps in merger shocks. Thus, one needs to invert the jump relations to give the merger shock velocities for a given shock temperature, pressure, and/or density increase. If the temperatures on either side of the merger shock can be measured from X-ray spectra, the shock velocity can be inferred from [22]

$$(63) \quad \Delta v_s = \left[\frac{kT_1}{\mu m_p} (C - 1) \left(\frac{T_2}{T_1} - \frac{1}{C} \right) \right]^{1/2},$$

where $\Delta v_s = v_1 - v_2 = [(C - 1)/C]v_s$ is the velocity change across the shock, and μ is the mean mass per particle in units of the proton mass m_p . The shock compression C

can be derived from the temperatures as

$$(64) \quad \frac{1}{C} = \left[\frac{1}{4} \left(\frac{\gamma+1}{\gamma-1} \right)^2 \left(\frac{T_2}{T_1} - 1 \right)^2 + \frac{T_2}{T_1} \right]^{1/2} - \frac{1}{2} \frac{\gamma+1}{\gamma-1} \left(\frac{T_2}{T_1} - 1 \right) \\ = \left[4 \left(\frac{T_2}{T_1} - 1 \right)^2 + \frac{T_2}{T_1} \right]^{1/2} - 2 \left(\frac{T_2}{T_1} - 1 \right).$$

Again, the second equation assumes $\gamma = 5/3$. Alternatively, the shock compression can be measured directly from the X-ray image. However, it is difficult to use measurements of the shock compression alone to determine the shock velocity, for two reasons. First, a temperature is needed to set the overall scale of the velocities; as is obvious from eq. (62), the shock compression allows one to determine the Mach number \mathcal{M} but not the shock velocity. The second problem is that temperature or pressure information is needed to know that a discontinuity in the gas density is a shock, and not a contact interface (e.g., the “cold fronts” discussed in § 6.2 below).

X-ray temperature maps of clusters have been used to derive the merger velocities using these relations. Reference [22] used ASCA observations to determine the kinematics of mergers in three clusters (Cygnus-A, Abell 2065, and Abell 3667). Because of the poor angular resolution of ASCA, these analyses were quite uncertain. More recently, possible shocks have been detected in Chandra images of a number of merging clusters (e.g., Abell 85 [85], Abell 665 [86], Abell 3667 [83]), and the shock jump conditions have been applied to determine the kinematics in these clusters.

The simplest case is a head-on symmetric merger at an early stage when the shocked region lies between the two cluster centers. Reference [22] suggests that the Cygnus-A cluster is an example. If the gas within the shocked region is nearly stationary, then the merger velocity of the two subclusters is just $v = 2\Delta v_s$. Applying these techniques to the ASCA temperature map for the Cygnus-A cluster, ref. [22] found a merger velocity of $v \approx 2200$ km/s. This simple argument is in reasonable agreement with the results of numerical simulations of this merger [87].

One can compare the merger velocities derived from the temperature jumps in the merger shocks with the values predicted by free-fall from the turn-around radius. In the case of Cygnus-A, [22] found good agreement with the the free-fall velocity of ~ 2200 km/s. This consistency suggests that the shock energy is effectively thermalized, and that a major fraction does not go into turbulence, magnetic fields, or cosmic rays. Thus, the temperature jumps in merger shocks can provide an important test of the relative roles of thermal and nonthermal processes in clusters of galaxies. (See the chapter by Rephaeli for more details.)

5.5. Nonequilibrium Effects. – Cluster mergers are expected to produce collisionless shocks, as occurs in supernova remnants. As such, nonequilibrium effects are expected, including non-equipartition of electrons and ions and nonequilibrium ionization [22, 88, 89]. Collisionless shocks are generally not as effective in heating electrons as ions.

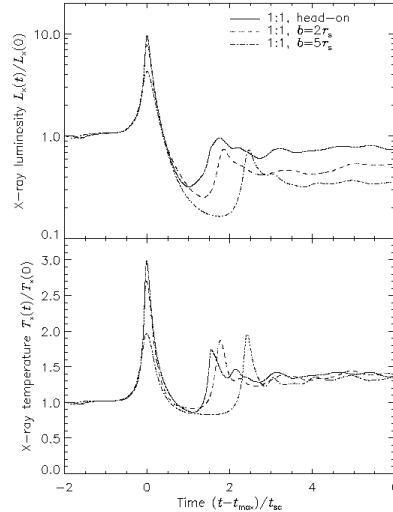


Fig. 9. – (Upper) Boost in the X-ray luminosity of a cluster of galaxies due to an equal mass merger, for a variety of impact parameters b [87, 19]. (Lower) Boost in the emission-weighted X-ray temperature for the same mergers.

Assuming that the post-shock electrons are somewhat cooler than the ions, the time scale for electron and protons to approach equipartition as a result of Coulomb collisions in a hot ionized gas is (eq. 13) [21]

$$\begin{aligned}
 (65) \quad t_{\text{equip}} &= \frac{3m_p m_e}{8\sqrt{2\pi} n_e e^4 \ln \Lambda} \left(\frac{kT_e}{m_e} \right)^{3/2} \\
 &\approx 2 \times 10^8 \left(\frac{T_e}{10^8 \text{ K}} \right)^{3/2} \left(\frac{n_e}{0.001 \text{ cm}^{-3}} \right)^{-1} \text{ yr},
 \end{aligned}$$

where n_e and T_e are the electron number density and temperature, respectively, and Λ is the Coulomb factor. The relative velocity between the post-shock gas and the shock front is $(1/4)v_s$; thus, one would expect the electron temperature to reach equipartition a distance of

$$(66) \quad d_{\text{equip}} \approx 160 \left(\frac{v_s}{3000 \text{ km/s}} \right) \left(\frac{T_e}{10^8 \text{ K}} \right)^{3/2} \left(\frac{n_e}{0.001 \text{ cm}^{-3}} \right)^{-1} \text{ kpc}$$

behind the shock front. Of course, it is the electron temperature (rather than the ion or average temperature) which determines the shape of the X-ray spectrum. This distance is large enough to insure that the lag could be spatially resolved in X-ray observations of low redshift clusters. Similar effects might be expected through non-equilibrium ionization.

On the other hand, it is likely that the nonequilibrium effects in cluster merger shocks are much smaller than those in supernova blast wave shocks because of the low Mach

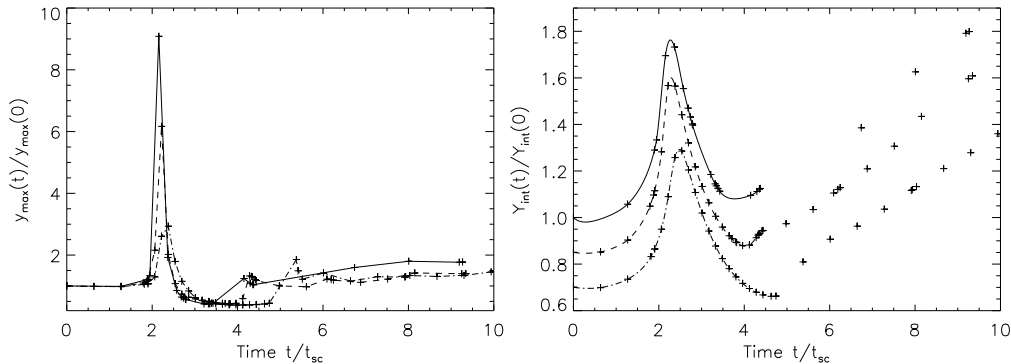


Fig. 10. – (Left) Boost in the central, maximum value of the SZ y parameter of a cluster of galaxies due to an equal mass merger, for a variety of impact parameters b [90]. The set of mergers are the same as in fig. 9. (Right) Boost in the integrated SZ parameter for the same mergers.

numbers of merger shocks. That is, the preshock gas is already quite hot (both electrons and ions) and highly ionized. Moreover, a significant part of the heating in low Mach number shocks is due to adiabatic compression, and this would still act on the electrons in the post-shock gas in merger shocks, even if there were no collisionless heating of electrons. For example, in a $\mathcal{M} = 2$, $\gamma = 5/3$ shock, the total shock increase in temperature is a factor of 2.08 (eq. 62). The shock compression is $C = 2.29$, so adiabatic compression increases the electron temperature by a factor of $C^{2/3} = 1.74$, which is about 83% of the shock heating.

5.6. Mergers Boosts to X-ray and SZ Measurements. – Mergers compress and heat the ICM, and thus can be expected to produce transient increases in their X-ray emission, temperature, and the SZ effect. Figure 9 illustrates the resulting X-ray boosts for several equal-mass mergers [87, 19]. The X-ray luminosity can be increased by as much as an order of magnitude by a major cluster merger. The X-ray temperature can be increased by a factor of ~ 3 . These merger boosts mean that the most X-ray luminous and hottest clusters will tend to be merging clusters. The cumulative effect of these “merger boosts” will affect the observed X-ray luminosity functions (XLFs) and temperature functions (TFs) of clusters. One expects this effect to be most important for the most luminous and hottest clusters. XLFs and TFs of clusters provide strong constraints on cosmological and large-scale-structure parameters, if these can serve as good proxies for the cluster mass function [19]. Merger boosts may limit the accuracy of the XLF and TF as cosmological probes. However, much of the effect of these boosts can be eliminated by the use of cluster mass proxies which depend less strongly on the densest and hottest regions of the cluster, such as the Y_X parameter [91].

Similar boosts are expected in the SZ effect from clusters [90]. (See the chapter by Rephaeli for more details concerning the SZ effect in clusters.) As shown in fig. 10, the

central SZ effect can be boosted by as much as an order of magnitude by a merger. However, the integrated SZ effect Y is affected much less dramatically. In fact, the merger boost to Y is generally less than the equilibrium change in Y due to the increase in mass of the cluster following the merger. Thus, mergers don't affect the large-scale SZ effect from clusters in a very dramatic way, and cosmological surveys based on these parameters should only be biased on the percent level or less.

5.7. Mergers and Basic Gravitational Physics Effects. – Merging clusters also provide several very direct tests of basic gravitational physics. These tests are possible because of the dynamical nature of mergers, and the difference in the behavior of collisional and non-collisional components of clusters. The gas in clusters is a collisional fluid (§ 3.3) with a mean-free-path which is small compared to the scale of clusters (eq. 22). Thus, when clusters collide, the motion of the gas will be retarded by ram pressure and shocks. On the other hand, the galaxies in clusters are essentially collisionless. When clusters collide, the galaxies will fly by one another. Thus, the galaxies in a merging subcluster will often be found ahead of the gas from the same subcluster. This is particularly obvious in late stage mergers with “cold fronts” (§ 6.2), where the gas which was initially at the center of a subcluster will be found lagging behind the central dominant and other galaxies from the subcluster. Perhaps the most prominent example of this is the “Bullet Cluster” 1E0657–56 [11, 12, 13], where the cold front and dense gas from the subcluster are clearly separated from the galaxies from the same subcluster.

In the most widely accepted model for “dark matter” (§ 3.6.4), the dominant component of the mass of the Universe is made up of collisionless elementary particles. For example, this would be true of Cold Dark Matter (e.g., [7]). If this is the case, one would expect that the dark matter would be located in the same regions of merging clusters as the galaxies. An alternative idea is that the laws of gravity or motion differ from the Newtonian form at large distances or small accelerations [92]. In these Modified Newtonian Dynamics (MOND) theories, there is no dark matter component of the Universe, and gravity is just due to ordinary baryonic matter. In clusters of galaxies, the vast majority of the ordinary baryonic matter is the hot X-ray gas (§ 3.6.4). Thus, MOND theories predict that in a merger, the gravity (or apparent dark matter) should mainly be located where the gas is located. In an advanced merger, the gas is located behind the galaxies.

The location of the gravity (or apparent dark matter) can be determined from weak gravitational lensing observations of the cluster [12, 13]. This test has been performed on the “Bullet Cluster” 1E0657–56 [12, 13], where the weak lensing measurements show that the gravity of the merging subcluster is centered on the galaxies, and is clearly displaced from the location of the subcluster gas. Thus, these measurements provide what is arguably the strongest proof of the existence of dark matter, rather than a change in the laws of gravity.

Another alternative to the conventional Cold Dark Matter hypothesis is that the dark matter consists of weakly interacting elementary particles, but the particles do have a small but significant cross-section for self-interaction [93]. If this were the case, the

dark matter would act as a collisional fluid, and would be displaced from the position of the galaxies in a merging cluster towards the center of the subcluster gas. In the “Bullet Cluster” 1E0657–56 no such displacement is evident [13], and the lack of such a displacement can be used to set an upper limit on the self-interaction cross-section per unit mass of dark matter of $< 1 \text{ cm}^2 \text{ g}^{-1}$. This is a very serious constraint on models of self-interacting dark matter.

6. – Mergers and Cool Cluster Cores

6.1. Cool Cores vs. Mergers. – The centers of a significant fraction of clusters of galaxies have luminous cusps in their X-ray surface brightness known as “cool cores” (§ 4; see also [42] for an extensive review). In every case, there is a bright (cD) galaxy at the center of the cool core region. The intracluster gas densities in these regions are much higher than the average values in the outer portions of clusters. X-ray spectra indicate that there are large amounts of gas at low temperatures (down to $\sim 10^7 \text{ K}$), which are much cooler than those in the outer parts of clusters. The high densities imply rather short cooling times t_{cool} (the time scale for the gas to cool to low temperature due to its own radiation). The primary observational characteristics of cool cores are very bright X-ray surface brightnesses which increase rapidly toward the center of the cluster.

Empirically, there is significant indirect evidence that mergers disrupt cool cores. There is a strong statistical anticorrelation between cool cores and/or cooling rates, and irregular structures in clusters as derived by statistical analysis of their X-ray images [94]. Looked at individually, very strong cooling cores are almost never associated with very irregular or bimodal clusters, which are likely merger candidates [95, 96]. There are some cases of moderate cool cores in merging clusters; in most cases, these appear to be early-stage mergers where the merger shocks haven’t yet reached the cooling core of the cluster. Examples may include Cygnus-A [22] and Abell 85 [85]. There also are a large number of merging clusters at a more advanced stage with relatively small cooling cores; Abell 2065 [22] may be an example. Recently, Chandra Observatory X-ray images have shown a number of merging clusters with rapidly moving cores of cool gas (the “cold fronts” discussed below in § 6.2). In these systems, the cool cores appear to have survived, at least to the present epoch in the merger.

It is unclear exactly how and under what circumstances mergers disrupt cool cores. The cool cores might be disrupted by tidal effects, by shock heating of the cooler gas, by removing the cool gas dynamically from the center of the cluster due to ram pressure, by mixing it with hotter intracluster gas, or by some other mechanism. Numerical hydrodynamical simulations are needed to study the mechanisms by which cool cores are disrupted. This is a relatively unexplored area, largely because the small spatial scales and rapid cooling time scales in the inner regions of cool cores are still a significant challenge to the numerical resolution of hydrodynamical codes. McGlynn and Fabian [97] argued that mergers disrupted cool cores, but this was based on purely N-body simulations. Hydrodynamical simulations have been made of the effects of head-on mergers with relatively small subclusters (1/4 or 1/16 of the mass of the main cluster) on a cool

core in the main cluster [98]. They find that the mergers disrupt the cool core in some cases, but not in others. Their simulations suggest that the disruption is not due to tidal or other gravitational effects.

Another possibility is that the merger shocks heat up the cool core gas and stop the gas from cooling. In the simulations, this does not appear to be the main mechanism of cool core disruption. There are a number of simple arguments which suggest that merger shocks should be relatively inefficient at disrupting cool cores. First, it is difficult for these shocks to penetrate the high densities and steep density gradients associated with cool cores, and the merger shocks would be expected to weaken as they climb these steep density gradients. Even without this weakening, merger shocks have low Mach numbers, and only produce rather modest increases in temperature (\lesssim a factor of 2). These small temperature increases are accompanied by significant compressions. As a result, shock heating actually decreases the cooling time due to thermal bremsstrahlung emission for shocks with Mach numbers $\mathcal{M} \leq (21 + 12\sqrt{3})^{1/2} \approx 6.5$. It is likely that the shocked gas will eventually expand, and adiabatic expansion will lengthen the cooling time. However, even if the gas expands to its preshock pressure, the increase in the cooling time is not very large. For a $\mathcal{M} = 2$ shock, the final cooling time after adiabatic expansion to the original pressure is only about 18% longer than the initial cooling time.

The simulations by [98] suggest that the main mechanism for disrupting cool cores is associated with the ram pressure of gas from the merging subcluster. The gas in the cool core is displaced, and may eventually mix with the hotter gas [87]. Earlier, [99] had argued that ram pressure, rather than shock heating, was the main mechanism for disrupting cool cores. Assuming this is the case, one expects that the merger will remove the cool core gas at radii which satisfy

$$(67) \quad \rho_{sc} v_{\text{rel}}^2 \gtrsim P_{\text{CF}}(r),$$

where $P_{\text{CF}}(r)$ is the pressure profile in the cool core, ρ_{sc} is the density of the merging subcluster gas at the location of the cool core, and v_{rel} is the relative velocity of the merging subcluster gas and the cool core. Reference [98] finds that this relation provides a reasonable approximation to the disruption in their simulations.

The pressure profile in the cool core gas prior to the merger is determined by the condition of hydrostatic equilibrium. If the cluster gravitational potential has a wide core within which the potential is nearly constant (e.g., as in a King model; eq. 8, fig. 1), then the cool core pressure will not increase rapidly into the center. In this case, once the merger reaches the central regions of the cluster, if the ram pressure is sufficient to remove the outer parts of the cool core, it should be sufficient to remove nearly all of the cool core. On the other hand, if the cluster potential is sharply peaked as is predicted by numerical simulations [14], the merger may remove the outer parts of the cool core but not the innermost regions. Thus, the survival and size of cool cores in merging clusters can provide evidence on whether clusters have sharply peaked potentials [22].

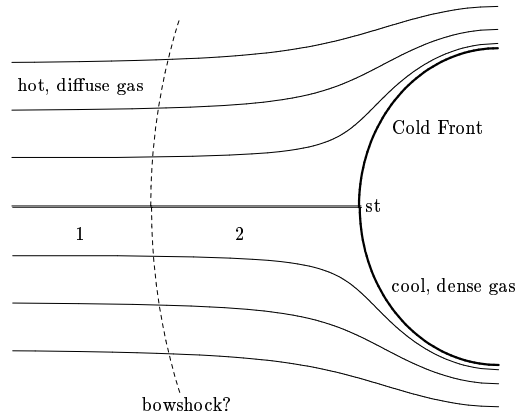


Fig. 11. – A schematic diagram of flow around a “cold front” in a cluster merger. The heavy solid arc at the right represents the contact discontinuity between the cold, dense cool core gas, and the hotter, more diffuse gas from the outer regions of the other cluster. The cool core is moving toward the left relative to the hotter gas. The narrow solid lines are streamlines of the flow of the hotter gas around the cool core. The region labelled “1” represent the upstream, undisturbed hot gas. If the cold front is moving transonically ($\mathcal{M}_1 > 1$), then the cold front will be preceded by a bow shock, which is shown as a dashed arc. The stagnation point, where the relative velocity of the cooler dense gas and hotter diffuse gas is zero, is marked “st”.

6.2. Cold Fronts. – One of the more dramatic early discoveries with the Chandra X-ray Observatory was the presence of very sharp surface brightness discontinuities in merging clusters of galaxies. A pair of such discontinuities were first seen in the public science verification data on the Abell 2142 cluster [100]. Initially, it seemed likely that these were merger shocks. However, temperature measurements showed that this was not the case. The high X-ray surface brightness regions were both dense and *cool*; thus, the gas in these regions had a lower specific entropy than the gas in the less dense regions. The lack of a pressure jump and the incorrect sign of the temperature and entropy variations showed that these features could not be shocks [100]. Instead, they appear to be contact discontinuities between hot, diffuse gas and a cloud of colder, denser gas [100]. In [83], these contact discontinuities were named “cold fronts.” Reference [100] argues that the source of the cold clouds are the cool cores of one or both of merging subclusters. As noted above, cool cores do appear to be able to partially survive in mergers, at least for some period. Subsequently, cold fronts have been observed in a number of other clusters; for an extensive review of the observations of these cold fronts, see [101].

6.2.1. Kinematics of Cold Fronts. As discussed extensively in [83], the variation in the density, pressure, and temperature of the gas in a cold front can be used to determine the relative velocity of cool core. This technique is analogous to that for merger shocks discussed above (eqs. 63 & 64). The geometry is illustrated in Figure 11, which is drawn in the rest frame of the cool core. We assume that the cool core has a smoothly curved, blunt front edge. The normal component of the flow of hot gas past the surface of the cool

core will be zero. There will be at least one point where the flow is perpendicular to the surface of the cool core, and the flow velocity of the hot gas will be zero at this stagnation point (“st” in Fig. 11). Far upstream, the flow of the hot gas will be undisturbed at the velocity of the cool core relative to the hotter gas, v_1 . Let c_{s1} be the sound speed in this upstream gas, and $\mathcal{M}_1 \equiv v_1/c_{s1}$ be the Mach number of the motion of the cool core into the upstream gas. If $\mathcal{M}_1 > 1$, a bow shock will be located ahead of the cold front.

The ratio of the pressure at the stagnation point to that far upstream is given by [25]

$$(68) \quad \frac{P_{\text{st}}}{P_1} = \begin{cases} (1 + \frac{\gamma-1}{2}\mathcal{M}_1^2)^{\frac{\gamma}{\gamma-1}}, & \mathcal{M}_1 \leq 1, \\ \mathcal{M}_1^2 (\frac{\gamma+1}{2})^{\frac{\gamma+1}{\gamma-1}} (\gamma - \frac{\gamma-1}{2\mathcal{M}_1^2})^{-\frac{1}{\gamma-1}}, & \mathcal{M}_1 > 1. \end{cases}$$

The ratio (P_{st}/P_1) increases continuously and monotonically with \mathcal{M}_1 . Thus, in principle, measurements of P_1 and P_{st} in the hot gas could be used to determine \mathcal{M}_1 . The pressures can be determined from X-ray spectra and images. In practice, the emissivity of the hot gas near the stagnation point is likely to be small. However, the pressure is continuous across the cold front, so the stagnation pressure can be determined just inside of the cool core, where the X-ray emissivity is likely to be much higher. Once \mathcal{M}_1 has been determined, the velocity of the encounter is given by $v_1 = \mathcal{M}_1 c_{s1}$.

If the motion of the cool core is transonic ($\mathcal{M}_1 > 1$), one can also determine the velocity from the temperature and/or density jump at the bow shock (eqs. 63 & 64). If the bow shock can be traced to a large transverse distance and forms a cone, the opening angle of this Mach cone corresponds to the Mach angle, $\theta_M \equiv \csc^{-1}(\mathcal{M}_1)$. However, variations in the cluster gas temperature may lead to distortions in this shape.

The distance between the stagnation point and the closest point on the bow shock (the shock “stand-off” distance d_s) can also be used to estimate the Mach number of the motion of the cold front [83]. The ratio of d_s to the radius of curvature of the cold front R_{cf} depends on the Mach number \mathcal{M}_1 and on the shape of the cold front. Figure 12 shows the values of d_s/R_{cf} as a function of $(\mathcal{M}_1^2 - 1)^{-1}$ for a spherical cold front [102]. Although there is no simple analytic expression for the stand-off distance which applies to all shapes of objects, a fairly general approximate method to calculate d_s has been given by [103]. and some simple approximate expressions exist for a number of simple geometries. The stand-off distance increases as the Mach number approaches unity; thus, this method is, in some ways, a very sensitive diagnostic for the Mach number for the low values expected in cluster mergers. On the other hand, the stand-off distance also depends strongly on the shape of the cold front as the Mach number decreases. The application of this diagnostic to observed clusters is strongly affected by projection effects. Because the radius of curvature of the bow shock is usually greater than that of the cold front, projection effects will generally cause d_s to be overestimated and \mathcal{M}_1 to be underestimated. Projection effects also make the true shape of the cold front uncertain.

These techniques have been used to determine the merger velocities from cold fronts in Abell 3667 [83], RXJ1720.1+2638 [104], and Abell 85 [85]. The most spectacular application is the “Bullet Cluster” 1E0657–56 [11, 12, 13], which contains a very high

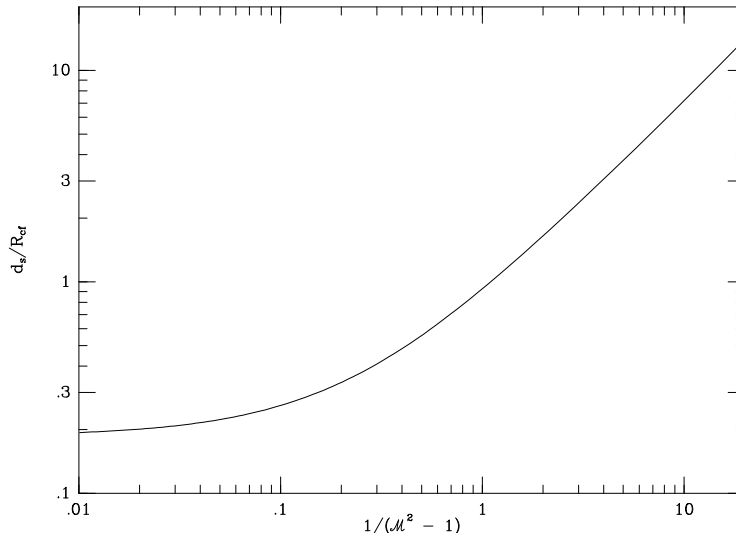


Fig. 12. – The ratio of the stand-off distance of the bow shock d_s to the radius of curvature R_{cf} of the stagnation region of the cold front, as a function of $1/(\mathcal{M}_1^2 - 1)$, where \mathcal{M}_1 is the Mach number. This is for a spherical cold front and $\gamma = 5/3$.

Mach number merger.

6.2.2. Width of Cold Fronts. One remarkable aspect of the cold fronts observed with the Chandra Observatory in several clusters is their sharpness. In Abell 3667, the temperature changes by about a factor of two across the cold front [83], and the accompanying change in the X-ray surface brightness occurs in a region which is narrower than 2 kpc [83]. This is less than the mean-free-path of electrons in this region. The existence of this very steep temperature gradient and similar results in other merging clusters with cold fronts requires that thermal conduction be suppressed by a large factor [105, 106, 83] relative to the classical value in an unmagnetized plasma (eq. 25) [21]. It is likely that this suppression is due to the effects of the intracluster magnetic field. It is uncertain at this point whether this is due to a generally tangled magnetic field (in which case, heat conduction might be suppressed throughout clusters), or due to a tangential magnetic field specific to the tangential flow at the cold front [106].

Because of the tangential shear flow at the cold front (Fig. 11), the front should be disturbed and broadened by the Kelvin-Helmholtz (K-H) instability. Reference [106] argues that the instability is suppressed by a tangential magnetic field, which is itself generated by the tangential flow. This suppression requires that the magnetic pressure P_B be a non-trivial fraction of the gas pressure P in this regions, $P_B \gtrsim 0.1P$. The required magnetic field strength in Abell 3667 is $B \sim 10 \mu\text{G}$. Alternatively, cold fronts might be stabilized by gravity [71] or acceleration along the front [107].

* * *

I would like to thank Alfonso Cavaliere and Yoel Rephaeli for organizing this excellent school, and the students for their interest and questions. I would also like to particularly thank the staff the school and of the Società Italiana di Fisica for their help, particularly when I had to visit the doctor in Varenna. This work was supported by Chandra grants TM7-8010X, AR7-8012X, GO7-8129X, GO7-8135X, and GO8-9083X, and by NASA XMM-Newton grants NNX06AE76G, NNX06AE75G, NNX08AZ34G, and NNX08AW83G, and by NASA Suzaku grants NNX06AI37G, NNX06AI44G, NNX08AI27G, and NNX08AZ99G.

REFERENCES

- [1] SARAZIN C. L., *X-ray emission from clusters of galaxies* (Cambridge Astrophysics Series, Cambridge: Cambridge University Press, 1988) 1988.
- [2] SARAZIN C. L., *Reviews of Modern Physics*, **58** (1986) 1.
- [3] VOIT G. M., *Reviews of Modern Physics*, **77** (2005) 207.
- [4] MCNAMARA B. R. and NULSEN P. E. J., *ARA&A*, **45** (2007) 117.
- [5] PLIONIS M., LOPEZ-CRUZ O. and HUGHES D., *A Pan-Chromatic View of Clusters of Galaxies and the Large-Scale Structure* (Springer, Dordrecht) 2008.
- [6] WHITE S. D. M., NAVARRO J. F., EVRARD A. E. and FRENK C. S., *Nature*, **366** (1993) 429.
- [7] BENNETT C. L., HILL R. S., HINSHAW G., NOLTA M. R., ODEGARD N., PAGE L., SPERGEL D. N., WEILAND J. L., WRIGHT E. L., HALPERN M., JAROSIK N., KOGUT A., LIMON M., MEYER S. S., TUCKER G. S. and WOLLACK E., *ApJS*, **148** (2003) 97.
- [8] VIKHLININ A., KRAVTSOV A., FORMAN W., JONES C., MARKEVITCH M., MURRAY S. S. and VAN SPEYBROECK L., *ApJ*, **640** (2006) 691.
- [9] SARAZIN C. L., *Gas Dynamics in Clusters of Galaxies*, in proc. of *A Pan-Chromatic View of Clusters of Galaxies and the Large-Scale Structure*, edited by PLIONIS M., LOPEZ-CRUZ O. and HUGHES D. (Springer, Dordrecht) 2008, pp. 1–30.
- [10] ZWICKY F., *ApJ*, **86** (1937) 217.
- [11] MARKEVITCH M., GONZALEZ A. H., DAVID L., VIKHLININ A., MURRAY S., FORMAN W., JONES C. and TUCKER W., *ApJ*, **567** (2002) L27.
- [12] CLOWE D., GONZALEZ A. and MARKEVITCH M., *ApJ*, **604** (2004) 596.
- [13] MARKEVITCH M., GONZALEZ A. H., CLOWE D., VIKHLININ A., FORMAN W., JONES C., MURRAY S. and TUCKER W., *ApJ*, **606** (2004) 819.
- [14] NAVARRO J. F., FRENK C. S. and WHITE S. D. M., *ApJ*, **490** (1997) 493.
- [15] CARLBERG R. G., YEE H. K. C., ELLINGSON E., MORRIS S. L., ABRAHAM R., GRAVEL P., PRITCHET C. J., SMECKER-HANE T., HARTWICK F. D. A., HESSER J. E., HUTCHINGS J. B. and OKE J. B., *ApJ*, **485** (1997) L13+.
- [16] POINTECOUTEAU E., ARNAUD M. and PRATT G. W., *A&A*, **435** (2005) 1.
- [17] BRYAN G. L. and NORMAN M. L., *ApJ*, **495** (1998) 80.
- [18] PRESS W. H. and SCHECHTER P., *ApJ*, **187** (1974) 425.
- [19] RANDALL S. W., SARAZIN C. L. and RICKER P. M., *ApJ*, **577** (2002) 579.
- [20] LACEY C. and COLE S., *MNRAS*, **262** (1993) 627.
- [21] SPITZER L. J., *Physics of Fully Ionized Gases* (Interscience, New York) 1956.
- [22] MARKEVITCH M., SARAZIN C. L. and VIKHLININ A., *ApJ*, **521** (1999) 526.
- [23] WISE M. W. and SARAZIN C. L., *ApJ*, **415** (1993) 58.
- [24] OSTERBROCK D. E., *Astrophysics of Gaseous Nebulae and Active Galactic Nuclei* (University Science, Mill Valley) 1989, pp. 53–65.

- [25] LANDAU L. D. and LIFSHITZ E. M., *Fluid Mechanics* (Pergamon, Oxford) 1959.
- [26] CAVALIERE A. and FUSCO-FEMIANO R., *A&A*, **49** (1976) 137.
- [27] VIKHLININ A., MARKEVITCH M., MURRAY S. S., JONES C., FORMAN W. and VAN SPEYBROECK L., *ApJ*, **628** (2005) 655.
- [28] MARKEVITCH M., FORMAN W. R., SARAZIN C. L. and VIKHLININ A., *ApJ*, **503** (1998) 77.
- [29] VOEVODKIN A. and VIKHLININ A., *ApJ*, **601** (2004) 610.
- [30] DAVÉ R., CEN R., OSTRICKER J. P., BRYAN G. L., HERNQUIST L., KATZ N., WEINBERG D. H., NORMAN M. L. and O'SHEA B., *ApJ*, **552** (2001) 473.
- [31] ALLEN S. W., SCHMIDT R. W., EBELING H., FABIAN A. C. and VAN SPEYBROECK L., *MNRAS*, **353** (2004) 457.
- [32] EKE V. R., NAVARRO J. F. and FRENK C. S., *ApJ*, **503** (1998) 569.
- [33] WHITE S. D. M. and FRENK C. S., *ApJ*, **379** (1991) 52.
- [34] KAISER N., *MNRAS*, **222** (1986) 323.
- [35] MARKEVITCH M., *ApJ*, **504** (1998) 27.
- [36] LOEWENSTEIN M., *ApJ*, **532** (2000) 17.
- [37] PONMAN T. J., CANNON D. B. and NAVARRO J. F., *Nature*, **397** (1999) 135.
- [38] LLOYD-DAVIES E. J., PONMAN T. J. and CANNON D. B., *MNRAS*, **315** (2000) 689.
- [39] PONMAN T. J., SANDERSON A. J. R. and FINOGUENOV A., *MNRAS*, **343** (2003) 331.
- [40] CAVALIERE A., LAPI A. and MENCI N., *ApJ*, **581** (2002) L1.
- [41] VOIT G. M. and BRYAN G. L., *Nature*, **414** (2001) 425.
- [42] FABIAN A. C., *ARA&A*, **32** (1994) 277.
- [43] NULSEN P. E. J., STEWART G. C., FABIAN A. C., MUSHOTZKY R. F., HOLT S. S., KU W. H.-M. and MALIN D. F., *MNRAS*, **199** (1982) 1089.
- [44] FABIAN A. C., NULSEN P. E. J., STEWART G. C., KU W. H.-M., MALIN D. F. and MUSHOTZKY R. F., *MNRAS*, **196** (1981) 35P.
- [45] COWIE L. L., HU E. M., JENKINS E. B. and YORK D. G., *ApJ*, **272** (1983) 29.
- [46] HECKMAN T. M., BAUM S. A., VAN BREUGEL W. J. M. and MCCARTHY P., *ApJ*, **338** (1989) 48.
- [47] CRAWFORD C. S., ALLEN S. W., EBELING H., EDGE A. C. and FABIAN A. C., *MNRAS*, **306** (1999) 857.
- [48] JOHNSTONE R. M., FABIAN A. C. and NULSEN P. E. J., *MNRAS*, **224** (1987) 75.
- [49] MCNAMARA B. R. and O'CONNELL R. W., *AJ*, **98** (1989) 2018.
- [50] HICKS A. K. and MUSHOTZKY R., *ApJ*, **635** (2005) L9.
- [51] SARAZIN C. L., BURNS J. O., ROETTIGER K. and MCNAMARA B. R., *ApJ*, **447** (1995) 559.
- [52] SALOMÉ P., COMBES F., EDGE A. C., CRAWFORD C., ERLUND M., FABIAN A. C., HATCH N. A., JOHNSTONE R. M., SANDERS J. S. and WILMAN R. J., *A&A*, **454** (2006) 437.
- [53] PETERSON J. R., KAHN S. M., PAERELS F. B. S., KAASTRA J. S., TAMURA T., BLEEKER J. A. M., FERRIGNO C. and JERNIGAN J. G., *ApJ*, **590** (2003) 207.
- [54] MORRIS R. G. and FABIAN A. C., *MNRAS*, **338** (2003) 824.
- [55] FABIAN A. C., ALLEN S. W., CRAWFORD C. S., JOHNSTONE R. M., MORRIS R. G., SANDERS J. S. and SCHMIDT R. W., *MNRAS*, **332** (2002) L50.
- [56] SOKER N., BLANTON E. L. and SARAZIN C. L., *A&A*, **422** (2004) 445.
- [57] WHITE D. A., FABIAN A. C., JOHNSTONE R. M., MUSHOTZKY R. F. and ARNAUD K. A., *MNRAS*, **252** (1991) 72.
- [58] BLANTON E. L., SARAZIN C. L., MCNAMARA B. R. and WISE M. W., *ApJ*, **558** (2001) L15.
- [59] BLANTON E. L., SARAZIN C. L. and MCNAMARA B. R., *ApJ*, **585** (2003) 227.

- [60] BURNS J. O., *AJ*, **99** (1990) 14.
- [61] TAYLOR G. B., FABIAN A. C. and ALLEN S. W., *MNRAS*, **334** (2002) 769.
- [62] SOKER N. and SARAZIN C. L., *ApJ*, **348** (1990) 73.
- [63] SARAZIN C. L., O'CONNELL R. W. and MCNAMARA B. R., *ApJ*, **389** (1992) L59.
- [64] BÖHRINGER H., VOGES W., FABIAN A. C., EDGE A. C. and NEUMANN D. M., *MNRAS*, **264** (1993) L25.
- [65] HUANG Z. and SARAZIN C. L., *ApJ*, **496** (1998) 728.
- [66] RIZZA E., LOKEN C., BLITON M., ROETTIGER K., BURNS J. O. and OWEN F. N., *AJ*, **119** (2000) 21.
- [67] FABIAN A. C., SANDERS J. S., TAYLOR G. B., ALLEN S. W., CRAWFORD C. S., JOHNSTONE R. M. and IWASAWA K., *MNRAS*, **366** (2006) 417.
- [68] MCNAMARA B. R., WISE M. W., NULSEN P. E. J., DAVID L. P., CARILLI C. L., SARAZIN C. L., O'DEA C. P., HOUCK J., DONAHUE M., BAUM S., VOIT M., O'CONNELL R. W. and KOEKEMOER A., *ApJ*, **562** (2001) L149.
- [69] CLARKE T. E., SARAZIN C. L., BLANTON E. L., NEUMANN D. M. and KASSIM N. E., *ApJ*, **625** (2005) 748.
- [70] YOUNG A. J., WILSON A. S. and MUNDELL C. G., *ApJ*, **579** (2002) 560.
- [71] FUJITA Y., SARAZIN C. L., KEMPNER J. C., RUDNICK L., SLEE O. B., ROY A. L., ANDERNACH H. and EHLE M., *ApJ*, **575** (2002) 764.
- [72] MCNAMARA B. R., NULSEN P. E. J., WISE M. W., RAFFERTY D. A., CARILLI C., SARAZIN C. L. and BLANTON E. L., *Nature*, **433** (2005) 45.
- [73] NULSEN P. E. J., MCNAMARA B. R., WISE M. W. and DAVID L. P., *ApJ*, **628** (2005) 629.
- [74] NULSEN P. E. J., HAMBRICK D. C., MCNAMARA B. R., RAFFERTY D., BIRZAN L., WISE M. W. and DAVID L. P., *ApJ*, **625** (2005) L9.
- [75] FROMMER C., ENSSLIN T. A. and SARAZIN C. L., *A&A*, **430** (2005) 799.
- [76] CHURAZOV E., SUNYAEV R., FORMAN W. and BÖHRINGER H., *MNRAS*, **332** (2002) 729.
- [77] BİRZAN L., RAFFERTY D. A., MCNAMARA B. R., WISE M. W. and NULSEN P. E. J., *ApJ*, **607** (2004) 800.
- [78] CROTON D. J., SPRINGEL V., WHITE S. D. M., DE LUCIA G., FRENK C. S., GAO L., JENKINS A., KAUFFMANN G., NAVARRO J. F. and YOSHIDA N., *MNRAS*, **365** (2006) 11.
- [79] VERNALEO J. C. and REYNOLDS C. S., *ApJ*, **645** (2006) 83.
- [80] BERTSCHINGER E., *ApJS*, **58** (1985) 39.
- [81] MINIATI F., RYU D., KANG H., JONES T. W., CEN R. and OSTRIKER J. P., *ApJ*, **542** (2000) 608.
- [82] RYU D., KANG H., HALLMAN E. and JONES T. W., *ApJ*, **593** (2003) 599.
- [83] VIKHLININ A., MARKEVITCH M. and MURRAY S. S., *ApJ*, **551** (2001) 160.
- [84] MARKEVITCH M., GOVONI F., BRUNETTI G. and JERIUS D., *ApJ*, **627** (2005) 733.
- [85] KEMPNER J. C., SARAZIN C. L. and RICKER P. M., *ApJ*, **579** (2002) 236.
- [86] MARKEVITCH M. and VIKHLININ A., *ApJ*, **563** (2001) 95.
- [87] RICKER P. M. and SARAZIN C. L., *ApJ*, **561** (2001) 621.
- [88] TAKIZAWA M., *ApJ*, **520** (1999) 514.
- [89] TAKIZAWA M., *ApJ*, **532** (2000) 183.
- [90] WIK D. R., SARAZIN C. L., RICKER P. M. and RANDALL S. W., *ApJ*, **680** (2008) 17.
- [91] KRAVTSOV A. V., VIKHLININ A. and NAGAI D., *ApJ*, **650** (2006) 128.
- [92] MILGROM M., *ApJ*, **270** (1983) 365.
- [93] SPERGEL D. N. and STEINHARDT P. J., *Physical Review Letters*, **84** (2000) 3760.
- [94] BUOTE D. A. and TSAI J. C., *ApJ*, **458** (1996) 27.
- [95] HENRIKSEN M. J., *ApJ*, **407** (1993) L13.

- [96] EDGE A. C., STEWART G. C. and FABIAN A. C., *MNRAS*, **258** (1992) 177.
- [97] MCGLYNN T. A. and FABIAN A. C., *MNRAS*, **208** (1984) 709.
- [98] GÓMEZ P. L., LOKEN C., ROETTIGER K. and BURNS J. O., *ApJ*, **569** (2002) 122.
- [99] FABIAN A. C. and DAINES S. J., *MNRAS*, **252** (1991) 17P.
- [100] MARKEVITCH M., PONMAN T. J., NULSEN P. E. J., BAUTZ M. W., BURKE D. J., DAVID L. P., DAVIS D., DONNELLY R. H., FORMAN W. R., JONES C., KAASTRA J., KELLOGG E., KIM D.-W., KOŁODZIEJCZAK J., MAZZOTTA P., PAGLIARO A., PATEL S., VAN SPEYBROECK L., VIKHLININ A., VRTILEK J., WISE M. and ZHAO P., *ApJ*, **541** (2000) 542.
- [101] FORMAN W., JONES C., MARKEVITCH M., VIKHLININ A. and CHURAZOV E., *High Angular Resolution Cluster Observations with Chandra: A New View*, in proc. of *Merging Processes in Galaxy Clusters*, edited by FERETTI L., GIOIA I. M. and GIOVANNINI G., Vol. 272 of *Astrophysics and Space Science Library* 2002, pp. 109–132.
- [102] SCHREIER S., *Compressible Flow* (Wiley, New York) 1982, pp. 182–189.
- [103] MOEKE W. E., *Approximate Method for Predicting Forms and Location of Detached Shock Waves Ahead of Plane or Axially Symmetric Bodies* (NASA Technical Note 1921, Washington) 1949.
- [104] MAZZOTTA P., MARKEVITCH M., VIKHLININ A., FORMAN W. R., DAVID L. P. and VANSPEYBROECK L., *ApJ*, **555** (2001) 205.
- [105] ETTORI S. and FABIAN A. C., *MNRAS*, **317** (2000) L57.
- [106] VIKHLININ A., MARKEVITCH M. and MURRAY S. S., *ApJ*, **549** (2001) L47.
- [107] CHURAZOV E. and INOGAMOV N., *MNRAS*, **350** (2004) L52.